

Institute for Hadronic Structure and Fundamental Symmetries

School of Natural Sciences

Technical University of Munich

Development of FPGA based frontend electronics for the scintillating fiber hodoscope of the AMBER experiment at CERN

Tim Maehrholz

Bachelor's Thesis

Abstract

The AMBER experiment at CERN aims to measure the proton radius by scattering muons on protons. The scintillating fiber hodoscope (SFH) is a key component of the PRM experiment, providing high precision time measurements of the incoming and scattered muons. The frontend electronics of the SFH, responsible for the detector readout, is FPGA-based and utilize the Citiroc1A ASIC for signal processing.

I developed the FPGA firmware for the control and readout of the Citiroc1A ASIC of the frontend electronics of the SFH.

I performed a threshold scan in order to characterize the frontend electronics and test the developed firmware.

The detailed structure of the firmware and the full characterization of the frontend electronics are presented in this thesis.

I conclude that the developed firmware is capable of controlling and reading out the signals from the Citiroc1A ASIC, but that the frontend electronics are currently not performing as desired. I propose further research and steps to investigate and understand the behaviour of the frontend electronics of the scintillating fiber hodoscope and complete it's development.

Contents

1. Introduction	1
2. The AMBER Experiment	3
2.1. Measurement of the Charge Radius of the Proton (PRM)	3
2.1.1. Previous Measurements of the Proton Radius	3
2.1.2. Elastic Scattering of Muons on Protons	3
2.2. General Setup for PRM at AMBER.	4
2.2.1. Detectors for PRM	4
2.2.2. Scintillating Fiber Hodoscope(SFH)	7
3. Frontend Electronic of the Scintillating Fiber Hodoscope	9
3.1. Field Programmable Gate Arrays (FPGA)	9
3.2. Overview of the Frontend Electronics	9
3.2.1. Processing of the SFH Signal	9
3.3. The Citroc1A ASIC	12
3.3.1. Signal Processing of the Citroc1A	12
3.3.2. Configuration of the Citroc1A	13
3.3.3. The iFTDC	18
4. Development of the FPGA Firmware for the SFH	19
4.1. Overview over the Firmware	19
4.1.1. The IPBUS Protocol	19
4.1.2. The Firmware Structure	20
4.2. The Address Space	21

Contents

4.3.	Configuration of the Citroc1A ASIC	22
4.3.1.	Status and Control Register	22
4.3.2.	Configuration State Machine	23
4.3.3.	Verification State Machine	25
4.4.	The Provisional Readout	26
4.5.	Testing the Firmware	26
4.5.1.	Setup for the Noise Measurement	26
4.5.2.	Theoretical Background for the Noise Measurement	28
5.	Measurement Results	31
5.1.	Noise Measurements	31
5.2.	Frontend Electronics Characterization	36
5.2.1.	Firmware Evaluation	36
5.2.2.	S-curve Analysis	37
5.2.3.	Comparison with Evaluation Board	40
5.2.4.	Behaviour at different Gain Setting	41
5.2.5.	Channel Behaviour Analysis	42
5.2.6.	Summary of the Characterisation	42
6.	Conclusion and Outlook	43
6.1.	Personal Contribution	43
6.2.	Conclusion	43
6.3.	Outlook	43
Appendix A.	Configurable Registers of the Citroc1A ASIC	45
Appendix B.	Fit Parameters of the S-Curve Analysis	53

CHAPTER 1

Introduction

”What we observe is not nature itself, but nature exposed to our method of questioning.”[Werner Heisenberg][9]

Progress in particle physics has always been driven by the desire to understand the fundamental building blocks of our universe.

Our current best theory for the inner workings of our world, the standard model of particle physics, tells us that the matter we see around us is mostly made up of down and up quarks and electrons. Combinations of these quarks, held together by the strong nuclear force, form the proton and neutron, the nuclei of the atoms that make up the matter of the everyday world[15]. Even though the proton was discovered over a century ago by Ernest Rutherford[13], it still holds several mysteries that continue to puzzle physicists. One of these mysteries is the size of the proton.

The semantic meaning of size in the realm of particle physics is not as straightforward as in the macroscopic world. An answer to the question, what is the size of the proton can be given by looking at the charge radius of the proton, first measured in 1956 by E. E. Chambers and R. Hofstadter[4].

Since then, the radius of the proton has been measured several times more with different methods, such as electron-proton scattering experiments and the lamb shift in muonic and ordinary hydrogen. The results of these measurements differ by five standard deviations, giving rise to the so called proton radius puzzle[1].

The proton radius measurement (PRM) experiment at AMBER at CERN aims at helping resolve this puzzle by measuring the proton radius with a new method, the elastic scattering of muons on protons.

To achieve this, the PRM experiment will measure the cross section of this scattering process and from this extract the form factors of the proton, which in turn allows for the calculation of the proton radius.

The scintillating fiber hodoscope (SFH) is a key component of the PRM experiment, as it provides precise time measurements of the incoming and scattered mouns, needed for particle distinction in pile-ups in the Pixel detectors[11].

This thesis will focus on the development of the FPGA driven frontend electronics of the scintillating fiber hodoscope (SFH), designed at the Technical University of Munich by the Physics Department E18 for the proton radius measurement at AMBER at CERN. Especially on the development of the FPGA firmware required for the control and readout of the Citiroc1A ASIC, a crucial part of the readout electronics.

The framework of this thesis is structured to provide the necessary background information for the development of the frontend electronics of the SFH.

The next chapter gives a general overview of the PRM experiment and the theoretical background of the proton radius measurement.

In chapter 3, the frontend electronics of the SFH, with a focus on the functionality and behaviour of Citiroc1A ASIC are described.

Chapter 4 explains the developed FPGA firmware for the control and readout of the Citiroc1A ASIC, and gives a short overview of the setup that was used for testing the developed firmware and characterizing the frontend electronics.

Chapter 5 presents the results of the testing of the developed firmware and the performance of the frontend electronics of the SFH.

The final chapter of this thesis gives a short summary of the results and an outlook on the future development of the frontend electronics of the SFH, necessary for it to successfully contribute to the resoluiton of the proton radius puzzle.

CHAPTER 2

The AMBER Experiment

2.1. Measurement of the Charge Radius of the Proton (PRM)

The proton is a baryon, a composite particle made up of one down and two up quarks. From this follows that the proton is not a point particle but has an internal structure[15]. The internal structure can be described by the structure functions of the proton, the electric and magnetic form factors G_E and G_M [1].

2.1.1. Previous Measurements of the Proton Radius

The charge radius of the proton has been measured several times using different methods. The two premier methods are electron proton scattering experiments and the Lamb shift in muonic and ordinary hydrogen. The results of these measurements differ by five standard deviations, as shown in Fig. 2.1, this has given rise to the so called proton radius puzzle[1].

2.1.2. Elastic Scattering of Muons on Protons

The AMBER PRM experiment at CERN aims at helping resolve the puzzle by measuring elastic scattering of muons on protons at high muon energies in the order of 100 GeV. The cross section at leading order, taking into account only interactions where one virtual photon was exchanged, for the elastic scattering of muons on a proton target is

$$\frac{d\sigma}{dQ^2} = \frac{\pi\alpha^2}{Q^4 m_p^2 p_\mu^2} \left[(G_E^2 + \tau G_M^2) \frac{4E_\mu^2 m_p^2 - Q^2(s - m_\mu^2)}{1 + \tau} - G_M^2 \frac{2m_\mu^2 Q^2 - Q^4}{2} \right] \quad (2.1)$$

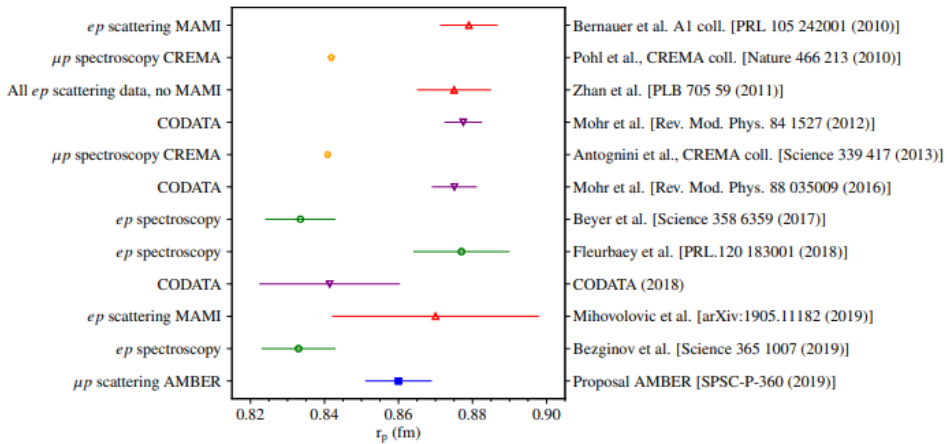


Figure 2.1.: Previous measurements of the proton radius from electron proton scattering experiments and the Lamb shift in muonic and ordinary hydrogen, the measurements differ from each other by five standard deviations. An arbitrary result for the proton radius by the PRM experiment, with the expected uncertainty, is included.[1]

with $Q^2 = -q^2$ the squared transferred four-momentum, $\tau = Q^2/4m_p^2$, $s = (p_\mu + p_p)^2$, G_E the electric form factor of the proton, G_M the magnetic form factor of the proton and α the fine structure constant[2]. Through determining the form factor G_E for small Q^2 , the charge radius of the Proton can be calculated with the following equation[2]

$$r_p^2 = -6 \frac{dG_E}{dQ^2} \Big|_{Q^2=0} \quad (2.2)$$

Since the cross section can not be measured at $Q^2 = 0$, the form factors G_E and G_M have to be extrapolated to $Q^2 = 0$. This is done by fitting the form factors to the experimental data and then extrapolating to $Q^2 = 0$ [2].

2.2. General Setup for PRM at AMBER.

2.2.1. Detectors for PRM

To determine the magnetic G_M and electric form G_E factors of the proton and thus the charge radius of the Proton, the experimental cross section of the elastic scattering of muons on protons has to be measured. The general setup of the PRM experiment, with a focus on the new detectors needed for the proton radius measurement, is shown in Fig. 2.2.

2.2. General Setup for PRM at AMBER.

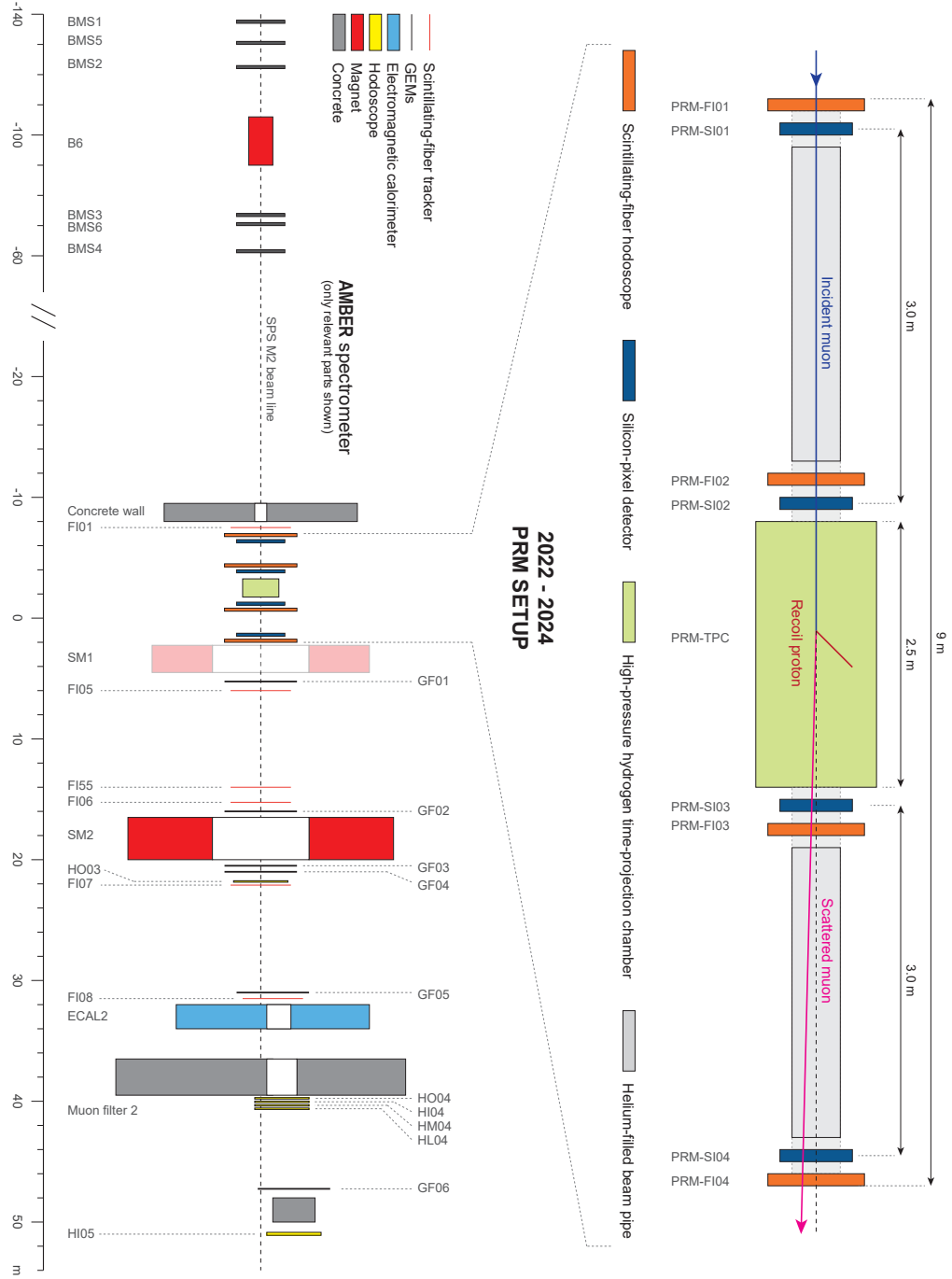


Figure 2.2.: General setup of the Amber experiment with new detectors for PRM[7]

The incoming muon beam with an energy of 100 GeV[1] and a beam rate of 2×10^6 [3] particles per second are scattered on a pressurized hydrogen gas target, located in the Time Projection Chamber (TPC), which also acts as the detector for the recoil path of the scattered proton.

The reconstruction of the path of the muon is achieved through the usage of two detector

types, combined into one unified tracking station (UTS) as shown in Fig. 2.3.

Each UTS consists of three layers of pixilated silicon detectors (ALPIDEs), for precise positional measurements (spatial resolution of about $8 \mu\text{m}$ ^[8]) of the incoming and scattered muons, but they lack, with their time uncertainty of $5 \mu\text{s}$ ^[8] the required time resolution for the PRM experiment. For this reason, each UTS includes a scintillating fiber hodoscope (SFH), the detector of interest for this thesis, which provides the time precision(300 ps ^[8]) for the measurement.

Four of these unified tracking stations, two before and two after the active target, are placed in the beamline as shown in Fig. 2.2. The measurement of the momentum of the scattered moun is done by existing COMPASS detectors located after the, for the PRM newly included detectors^[1].

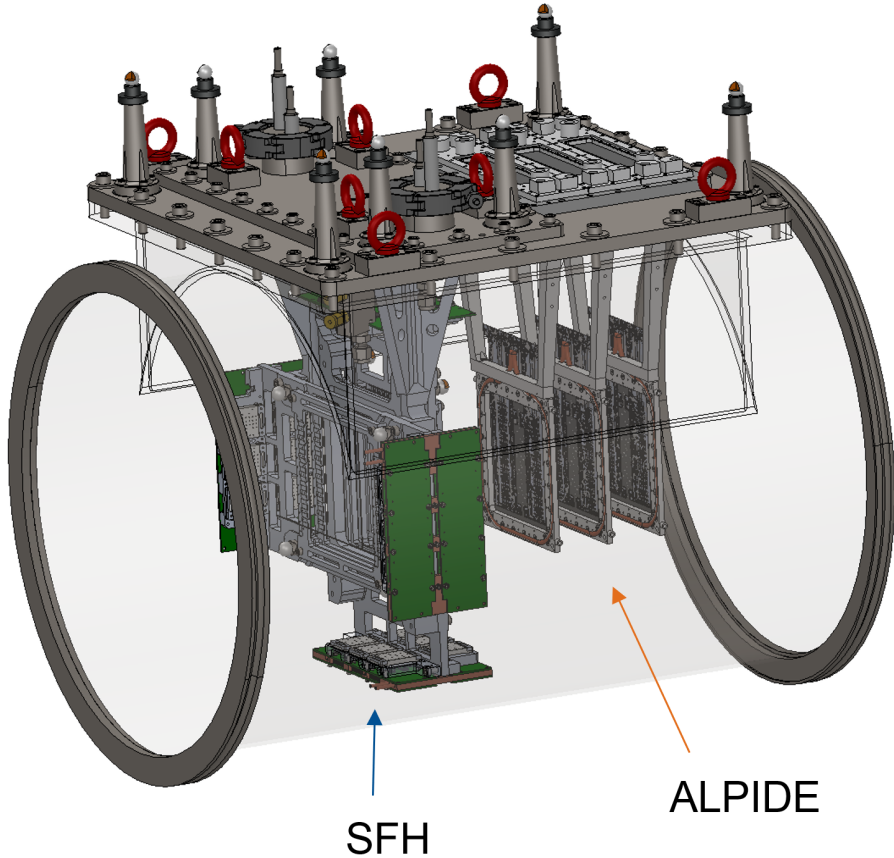


Figure 2.3.: Unified tracking station (UTS) with three layers of pixilated silicon detectors (ALPIDEs) and the scintillating fiber hodoscope (SFH)^[7]

2.2.2. Scintillating Fiber Hodoscope(SFH)

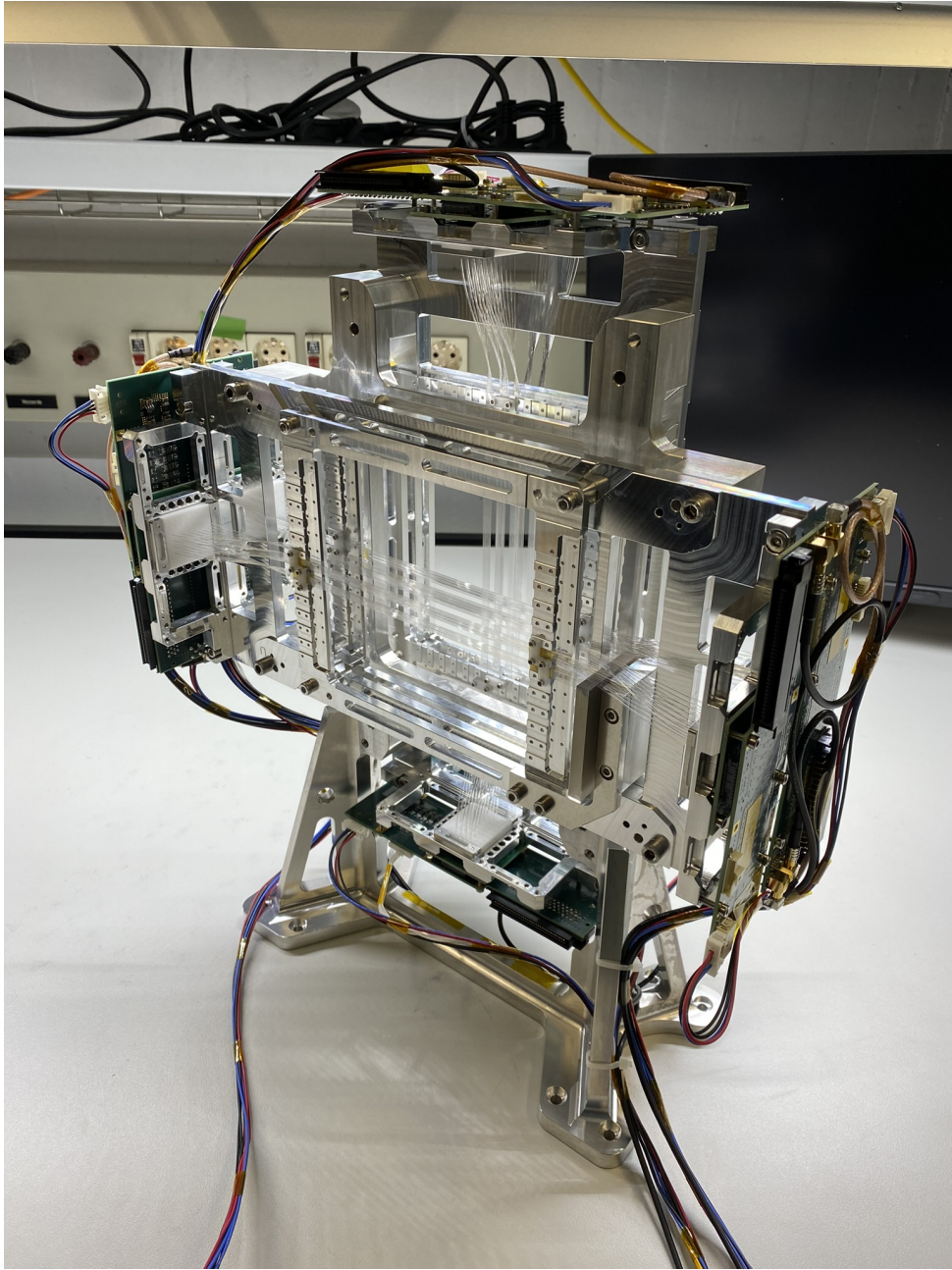


Figure 2.4.: Scintillating fiber hodoscope (SFH) with two of the four layers of scintillating fibers installed. The frontend electronics is not attached[7]

The scintillating fiber hodoscope shown in Fig. 2.4, the detector for which the FPGA driven frontend electronics is developed in this thesis, is used to measure the precise timing(300 ps[8]) of the incoming and scattered muons. Every SFH contains four layers of scintillating fibers, two in x and two in y direction. Each layer is made up of 192[8], 500 μm thick[5] fibers, in total 768[8] fibers per SFH. When charged particles, muons, in this

case, pass through a scintillating fiber they excite the scintillating material, which then emits photons. One end of every fiber are connected to a silicon photomultiplier (SiPM), which converts the photons into an electrical signal that is then processed by the frontend electronics[7].

CHAPTER 3

Frontend Electronic of the Scintillating Fiber Hodoscope

3.1. Field Programmable Gate Arrays (FPGA)

The frontend electronics for the scintillating fiber hodoscope (SFH) is based on Field Programmable Gate Arrays (FPGAs). Field Programmable Gate Arrays (FPGAs) are integrated circuits that can be programmed after manufacturing. FPGA are made up of a grid of programmable logic blocks (PLBs) and programmable interconnects. They possess the advantage of being flexible, reconfigurable and able to process large amounts of data in parallel. The frontend electronics for the SFH require large amounts of data to be processed in real time, which makes FPGAs, with their large data throughput and parallel processing capabilities, ideal for this task[6].

The FPGA used in the frontend electronics for the scintillating fiber hodoscope is part of the Xilinx Artix-7 family[11].

3.2. Overview of the Frontend Electronics

3.2.1. Processing of the SFH Signal

The frontend electronics of the scintillating fiber hodoscope process the signals from the scintillating fibers. They are attached on all four sides of the SFH, as shown in Fig. 2.4. Two types of readout are considered for the SFH, a mirrored readout and a non-mirrored readout. In the mirrored scenario, only one end of the fibers is connected to the SiPM array and the other end is mirrored, while in the non mirrored readout, both ends are

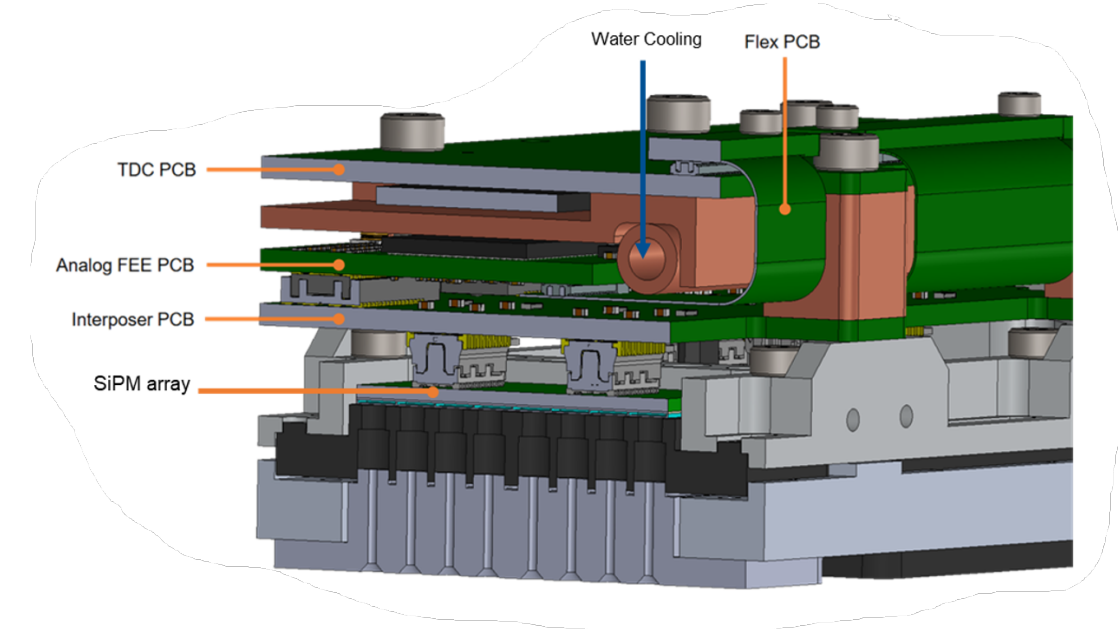


Figure 3.1.: Sideview of the frontend electronics that will be attached on the sides of the SFH, the fiber holders will be attached to the fibers[7]

connected[7].

The mirrored scenario has the advantage of only requiring 4 instead of 8 frontend electronics units, halving the number of channels and thus the amount of data that has to be processed. Furthermore, test beam measurements show that the mirrored readout has a higher efficiency than the non-mirrored readout[11].

Due to these advantages, currently, the mirrored configuration is planned for the SFH[7]. Each SFH possesses 768 fibers, and for the mirrored configuration, this results in 768 signals that have to be processed, spread out over 4 frontend electronics units, each handling 192 signals.

The fibers are connected to the fiber holders as shown in Fig. 3.1. The incoming photons are converted into electric signals by the SiPM arrays.

These are then transmitted to the heart of the frontend electronics via the interposer PCB, also shown in Fig. 3.1.

The heart of the frontend electronics is made up of two components, the FEE PCB and iFTDC, stacked on top of each other, connected by three flex PCBs and plug connectors.



Figure 3.2.: The analog frontend electronics (FEE) PCB with the six Citiroc1A ASICs. The output of the Citiroc1A ASICs is transmitted to the iFTDC over three flex PCBs[7]

The analog frontend electronics (FEE), illustrated in Fig 3.2, incorporates six Citiroc1A ASICs, each handling 32 channels. The SiPM signals are amplified, shaped and discriminated by the Citiroc1A ASICs and then transmitted to the iFTDC over the three flex PCBs.

The FPGA housed on the iFTDC, described in Section 3.3.3, reads these signals out and processes them, as well as controlling the Citiroc1A ASICs with the signals shown in Fig. 3.3[11].

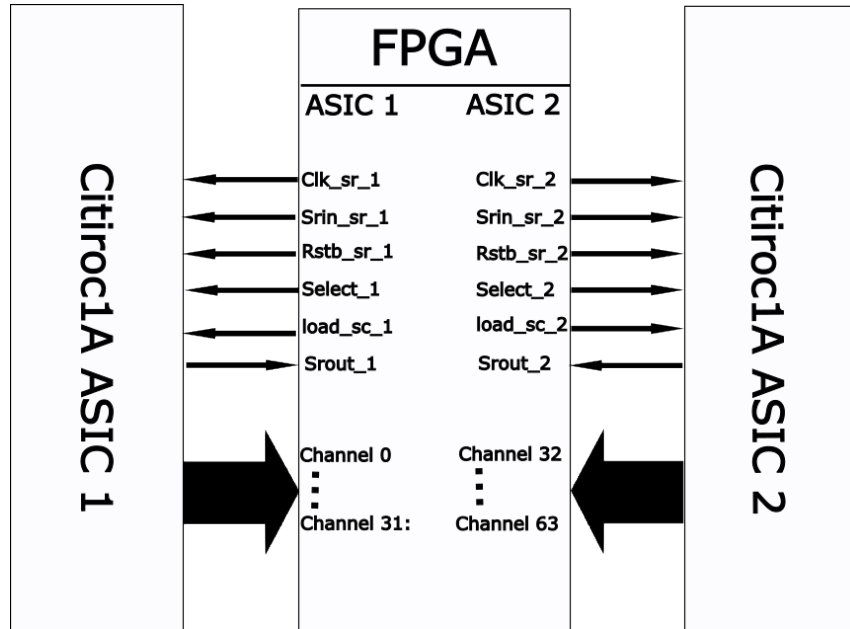


Figure 3.3.: The signals used by the FPGA to control and readout the two Citiroc1A ASICs[14]

3.3. The Citiroc1A ASIC

The Citiroc1A ASIC is an Application-Specific Integrated Circuit developed by Weeroc company for the readout of SiPM detectors. It allows for the readout of 32 channels and is sensitive to $\frac{1}{3}$ of a photoelectron[14].

3.3.1. Signal Processing of the Citiroc1A

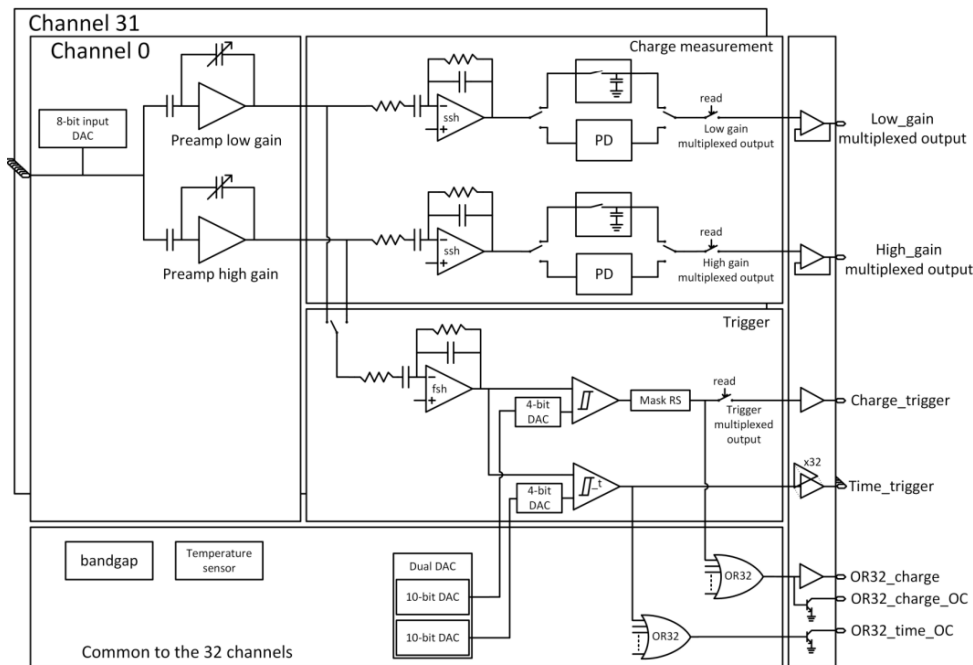


Figure 3.4.: General ASIC block scheme of the Citiroc1A[14]

The general block scheme of the Citiroc1A is shown in Fig. 3.4.

The Citiroc1A allows fine tuning of the SiPM bias voltage for each channel via the 8-bit input DAC.

The input signals are amplified with a for every channel configurable high or low gain by an integrator as depicted in Fig. 3.5. The feedback capacitance of for the high gain is adjustable from 25 fF to 1575 fF in 25 fF steps, via a 6 bit dac, with the feedback capacitance following equation 3.1

$$\text{feedback capacitance} = (63 - \text{Dac_value}) \times 25 \text{ fF} \quad (3.1)$$

and the resulting voltage amplification equation3.2

$$\frac{V_{\text{out}}}{V_{\text{in}}} = \frac{15 \text{ pF}}{\text{feedback capacitance}} = 600 \times \frac{1}{63 - \text{Dac_value}} \quad (3.2)$$

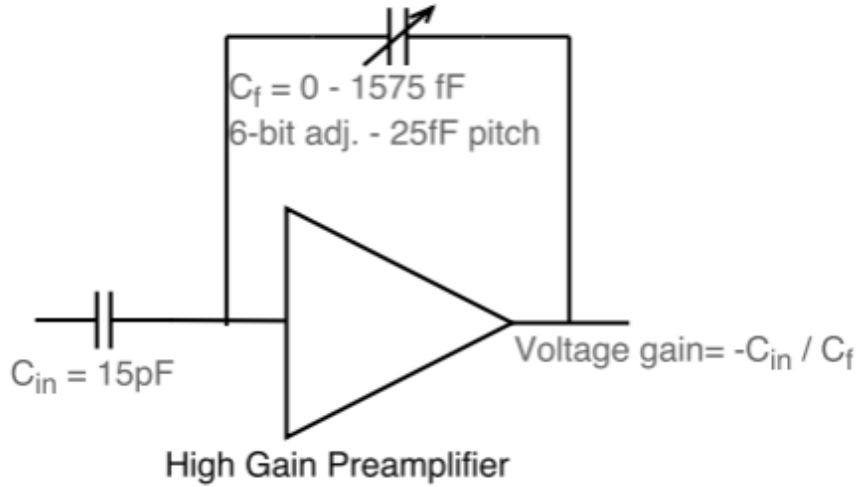


Figure 3.5.: High gain amplification of the Citiroc1A. The feedback capacitance is adjustable from 25 fF to 1575 fF in 25 fF steps[14]

[14]

The PRM experiment requires the maximal high gain of 62 amplifying the incoming voltage by a factor 600[11].

The amplified signals are then shaped by either the slow (ssh) or fast shaper (fsh), as shown in Fig. 3.4. The fast shaper is used for the PRM experiment since it has a better time resolution, which is important for the SFH performance[14].

Each channel of the ASIC has two discriminators, namely the charge discriminator and the time discriminator. In this thesis, i discuss only the time discriminator, since it provides the time information. The time discriminator threshold is adjustable via a 10-bit dac for all channels and an additional 4-bit dac for every channel individually, as shown in Fig. 3.4[14].

3.3.2. Configuration of the Citiroc1A

The configuration of the Citiroc1A is achieved by the FPGA via the five signals shown in Fig. 3.6. The **Select** signal allows the choice between configuring the slow control, for **Select** = 1 or the probe register, for **Select** = 0[14].

The Slow Control Register

The slow control register is used to set values for internal variables like the high gain for a channel or the time discriminator threshold. It also allows the FPGA to turn off specific stages of the Citiroc1A, such as the slow shaper or the time discriminator. The register is

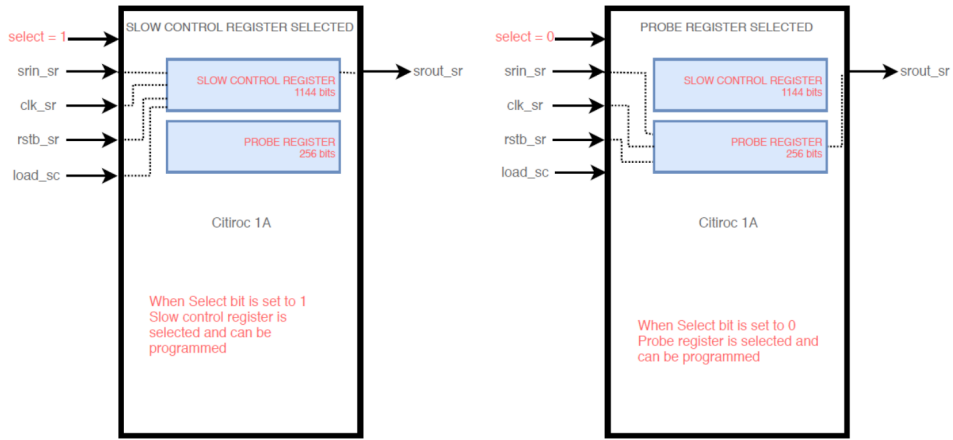


Figure 3.6.: The two configurable registers of the Citiroc1A are selected using the **Select** signal. The FPGA communicates with the Citiroc1A through the signals **Clk_sr**, **Rstb_sr**, **Srin_sr**, and **Load_sr**, while the **Srout** signal is sent back from the Citiroc1A to the FPGA for verification[14]

1144 bits long. A complete list of all the registers of the slow control is shown in table A.1 in appendix A.

The process of writing the bitstream into the slow control register by the FPGA is illustrated in Fig. 3.7.

The **Rstb_sr** signal is an asynchronous active-high reset for the serial register, applying to both the slow control and probe register.

The FPGA processes the bitstream sequentially, starting with the least significant bit (LSB). The first bit of the bitstream to enter the serial register will be the last bit of the slow control register. Each bit is sent on the **Srin_sr** signal in coordination with a rising edge of the **Clk_sr** clock signal.

The **Load_sr** signal is used to load the bitstream into the slow control register. After all bits have been sent to the Citiroc1A, a rising edge on **Load_sr** is required to load the slow control register.

The **Srout** signal is sent back from the Citiroc1A to the FPGA for bitstream verification. Only after the FPGA has sent the full bitstream twice does the **Srout** signal take on the value of the bitstream, since the **Srout** signal is shifted by the length of the bitstream[14]. One should only set the rising edge of the **Load_sr** signal after verifying that the **Srout** signal takes on the correct values.

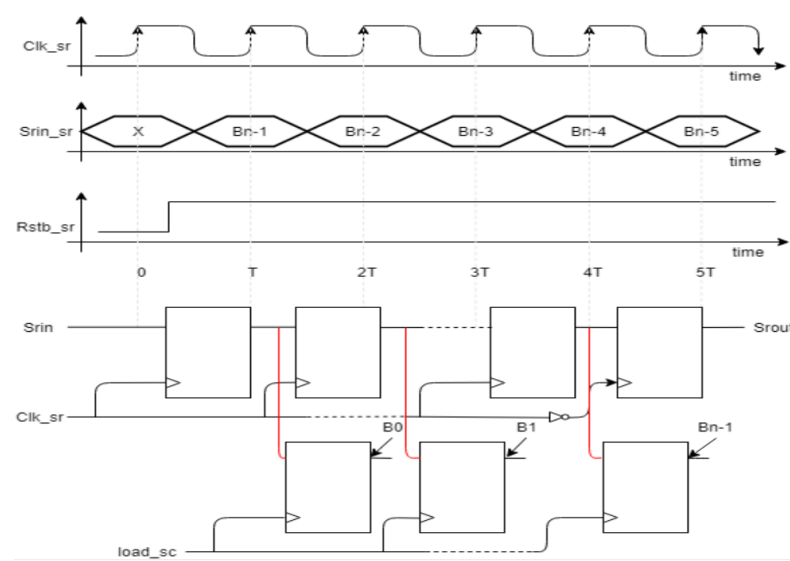


Figure 3.7.: The slow control chronogram, depicting the bitstream writing process controlled by **Clk_sr** the clock signal and **Srin_sr** the data signal. A rising edge of **Load_sc** is required after successful verification with the **Srouut** signal to load the slow control register[14]

The Probe Register

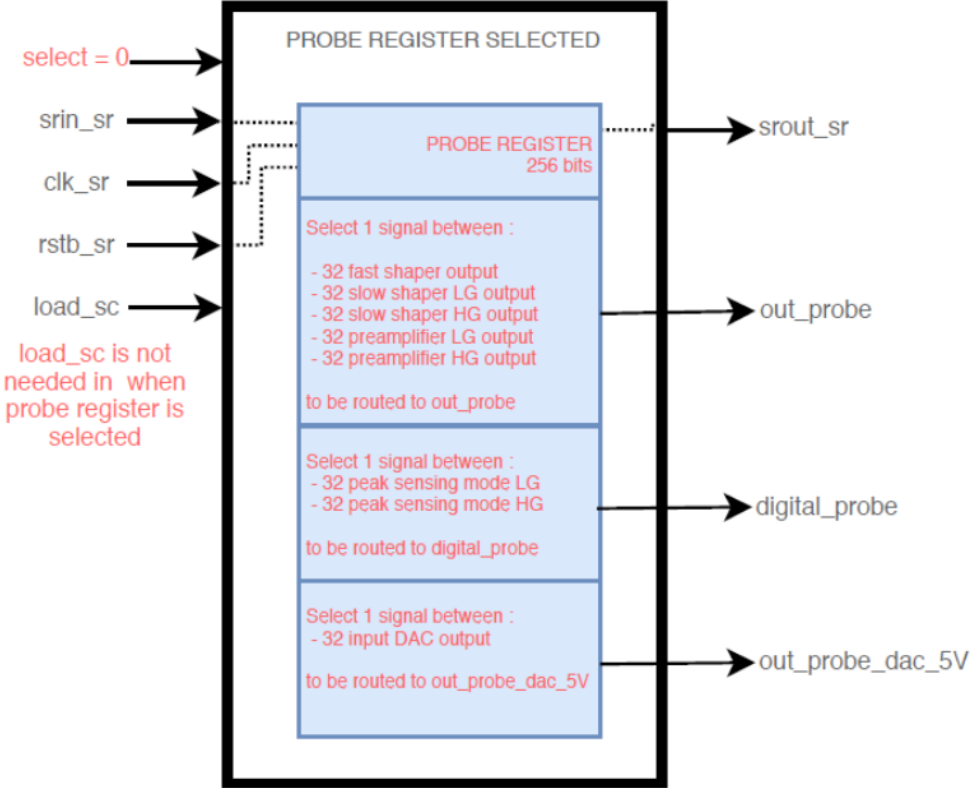


Figure 3.8.: Scheme block of internal probing system, allowing the routing of internal signals to probe pins for debugging purposes. It is configured via the probe register[14]

The probe register is used to route internal signals to several output pins for debugging purposes. Its functionality is illustrated in Fig. 3.8. The register consists of 256 bits and is written the same way as the slow control register, with the difference that the bits are directly written into the Citiroc1A without requiring a rising edge on Load_sc[14].

The complete list of the probe register is shown in table A.2 in appendix A.

The internal signals for each channel that can be routed to the output pins are shown in table 3.1.

3.3. The Citiroc1A ASIC

Signal Source	Description	Output Pin
High and low gain preamplifier, slow and fast shapers	Outputs of preamplifiers and shapers	out_probe
PeakSensing_modeb_LG	Internal peak-sensing signal for low gain	digital_probe
PeakSensing_modeb_HG	Internal peak-sensing signal for high gain	-
Output of input DAC	DAC output voltage (5 V)	out_probe_dac_5_V

Table 3.1.: Internal signal routing to output pins for each channel[14].

Only one signal can be routed to each output pin at a time without potentially causing a short circuit[14].

3.3.3. The iFTDC



Figure 3.9.: The iFTDC with three Artix-7 FPGA, the three flex PCBs that connect the iFTDC with the FEE PCB and the connected power supply.

The iFTDC, depicted in Fig. 3.9, is a FPGA based time-to-digital converter. It houses three Artix-7 FPGA. Each FPGA handles the readout as well as the control of two of the Citiroc1A ASICs[11].

The FPGA firmware is loaded via jtag. The control and readout of the FPGAs is performed via Ethernet.

CHAPTER 4

Development of the FPGA Firmware for the SFH

4.1. Overview over the Firmware

The firmware of the different FPGAs differs only by their port assignment, but otherwise are identical.

The firmware must fulfill several functionalities.

The main tasks of the firmware are to configure the Citroc1A ASICs, explained in section 3.3.2, communication with the controlling computer via Ethernet and the IPBUS protocol and a provisional readout of the time triggered data from the Citroc1A ASICs. The firmware is written in VHSIC Hardware Description Language (VHDL) and is synthesized and implemented using Xilinx Vivado. Several IP-cores, provided by Xilinx, are used to simplify the development of the firmware for several tasks like the implementation of the configuration memory.

4.1.1. The IPBUS Protocol

The IPBUS protocol used for the communication between the FPGA and the controlling computer is a simple protocol for controlling IP-aware hardware devices with a 32-bit read and write bus using UDP as the transport protocol[12].

The IPBUS protocol defines a read and write command enabling successful write and read operations of a 32-bit register with a 32-bit address in the FPGA.

The commands can be issued on the controlling computer with the μ HAL library, which allows the user to issue read and write commands using a python script and an XML file

defining the addresses of the registers[12].

The address space inside the FPGA is defined in the firmware.

4.1.2. The Firmware Structure

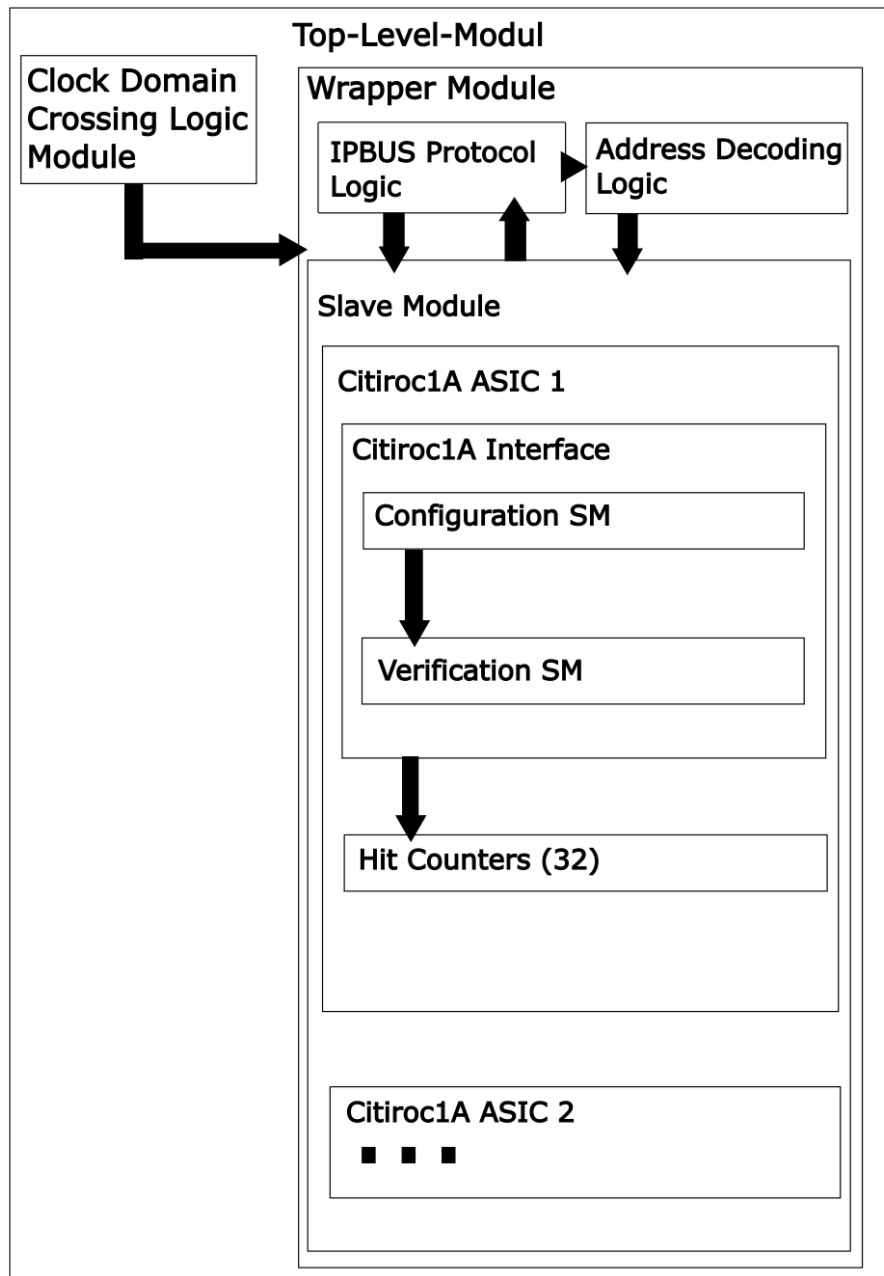


Figure 4.1.: Hierarchical structure of the firmware, where each module contains its sub-modules. The black arrows indicate connections that are semantically correct but are routed through higher-level modules.

The firmware has a hierarchical structure illustrated in Figure 4.1.

The top level module of the firmware defines the interconnections between internal FPGA

logic and external components such as the Ethernet transceiver, clock oscillators and Citiroc1A ASICs.

The FPGA logic includes an IPBUS IP core and the slave entities in addition to a Clock Crossing Domain logic module which synchronizes the time triggered Citiroc1A signals.

The slave module contains two identical Citiroc1A modules, one for each ASIC. The Citiroc1A interface is instantiated for the configuration and verification of the ASIC. The hit counters allow to perform hit rate measurements for the 32 channels of the Citiroc1A ASIC.

4.2. The Address Space

The 32-bit address is divided into sub addresses by the address decoding logic of the firmware.

The address space is first divided between the two Citiroc1A ASICs:

Citiroc1A Interface ASIC 1:	0000_0000_0000_0000_0 001 _0000_0000
Citiroc1A Interface ASIC 2:	0000_0000_0000_0000_0 010 _0000_0000
Hit counters of ASIC 1:	0000_0000_0000_0000_0 011 _0000_0000
Hit counters of ASIC 2:	0000_0000_0000_0000_0 100 _0000_0000

The address space of the Citiroc1A Interface is further divided into the following sub addresses:

Status and Control Register:	0000_0000_0000_0000_0 000 _0000
Configuration RAM:	0000_0000_0000_0000_0 0100 _0000
Verification RAM:	0000_0000_0000_0000_0 1000 _0000

To read the second address of the configuration RAM of the first Citiroc1A ASIC, the address would be:

0000_0000_0000_0000_0001_0100_0001

The address space of the hit counters is also further divided into sub addresses:

Hit counter 0:	0000_0000_0000_0000_0000_0 0000 _0001
Time counter 0:	0000_0000_0000_0000_0000_0 0100 _0001
Hit counter 1:	0000_0000_0000_0000_0000_0 0000 _0010
Time counter 1:	0000_0000_0000_0000_0000_0 0100 _0010
...	...
Hit counter 31:	0000_0000_0000_0000_0000_0 0001 _1111
Time counter 31:	0000_0000_0000_0000_0000_0 0101 _1111

The address to read the time counter of the fifth channel of the second Citiroc1A ASIC would be:

0000_0000_0000_0000_0100_0100_0101

4.3. Configuration of the Citiroc1A ASIC

The configuration of the slow control and probe registers of the Citiroc1A ASIC, along with the verification of this configuration, is handled by two finite state machines.

Each state machine controls a random access memory (RAM) with a depth of 64 addresses, with each address storing 32-bits of data.

The state machines, in turn, are controlled by the status and control register of the corresponding Citiroc1A Interface, which can be written by the controlling computer via the IPBUS protocol.

4.3.1. Status and Control Register

Each Citiroc1A interface has a 32-bit status and control register, but only the first 7 bits are used. It is responsible for the control of the configuration and verification state machines as well as the hit counters. The bits of the status and control register, with the exception of bit 1 do not reset themselves after being set to 1 and have to be deasserted by the controlling computer.

Bit 1 is set to 0 by the FPGA after the configuration is loaded into the serial register. Its structure is shown in table 4.2.

Bit	Description
bit 0	Selects between slow control (1) and probe register (0)
bit 1	Loads the configuration into the serial register
bit 2	Resets the Configuration and Verification SM and the Configuration RAM
bit 3	Resets the Citiroc1A serial register
bit 4	Loads the configuration into the slow control register
bit 5	Resets the hit counters associated with the Citiroc1A
bit 6	Enables the hit counters associated with the Citiroc1A

Figure 4.2.: Structure of the status and control register of the Citiroc1A interface. The specified commands are executed when the bits are set to 1.

4.3.2. Configuration State Machine

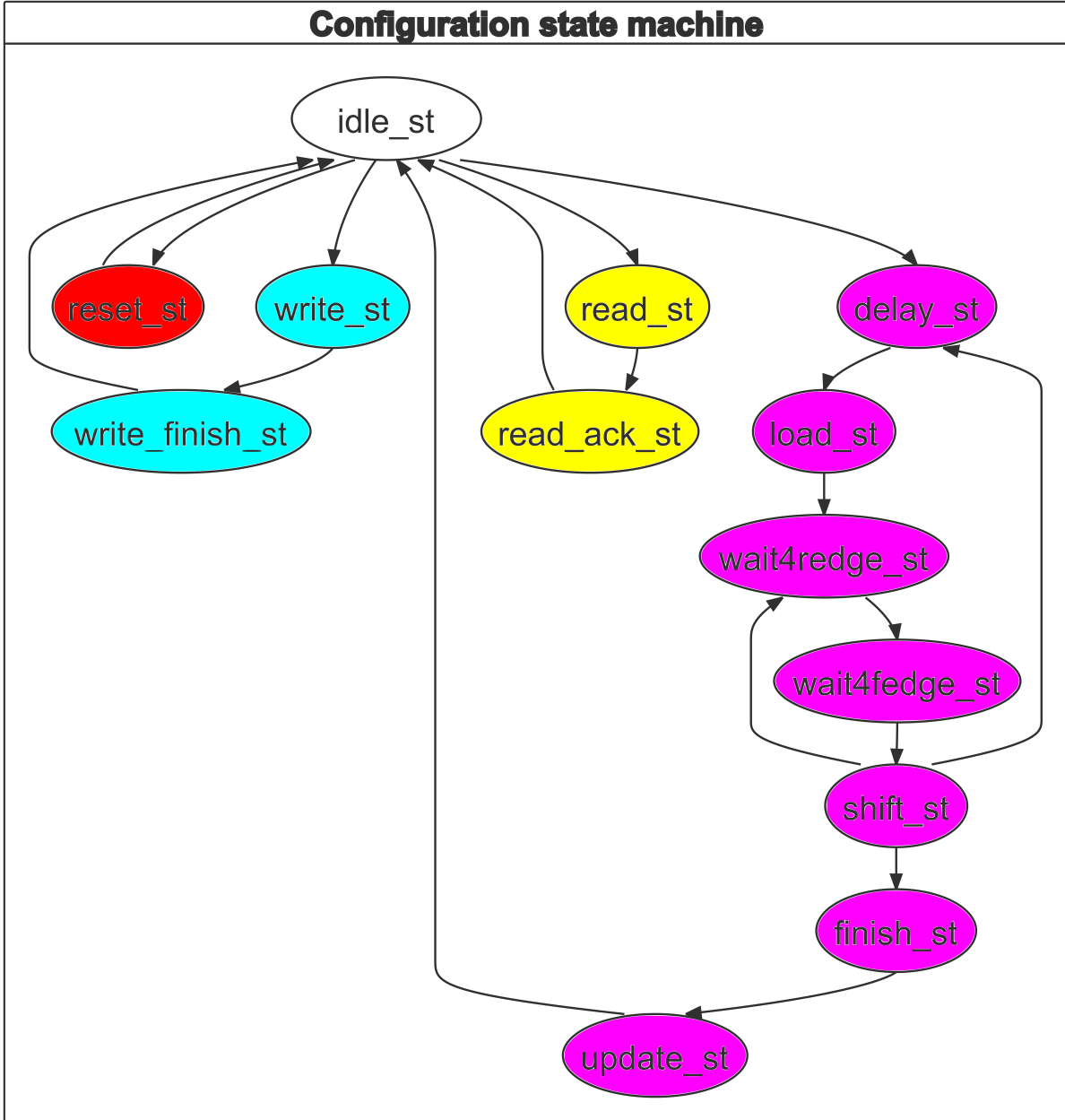


Figure 4.3.: Finite state machine for configuring the Citiroc1A ASIC. States associated with the same processes are highlighted using the same color.

The Configuration state machine, embedded in the firmware, as shown in Fig. 4.1, is responsible for configuring the slow control and probe registers of the Citiroc1A ASIC. The state machine is controlled by the status and control register, which is written by the controlling computer via the IPBUS protocol. It has four processes, whose states are shown in different colors in Fig. 4.3.

The **write** process is responsible for writing the configuration data to the configuration

RAM. 32-bits can be written to a specified address in the configuration RAM at a time by the controlling computer.

The **read** process allows the controlling computer to read the content of the configuration RAM at the specified address.

The **reset** process resets the configuration RAM and the Configuration state machine and is initiated by setting bit 2 of the status and control register to 1.

The **load** process loads the configuration data from the configuration RAM into the serial register of the Citiroc1A ASIC. The first 1144/256 bits of the configuration RAM are shifted into the serial register of the Citiroc1A ASIC, depending on the selected register. Each bit is shifted in by setting the data line **Srin_sr** and clock **clk** as described in section 3.3.2. As described in section 3.3.2, the first bit written to the serial register is the last bit of the configuration, the controlling computer has to write the bitstream in reverse order to the configuration RAM.

The **clk** clock signal for the ASIC's serial register is generated by the FPGA with a frequency of 1 MHz. The **load** process modulates this clock signal to control the operation of the serial register.

The process is repeated until all the data is shifted in and the configuration is loaded. It can be initiated by the controlling computer by setting bit 1 of the status and control register to 1 and is only interruptible by the **reset** process.

In order to load the configuration into the slow control register from the serial register, bit 4 of the status and control register must be set to 1, this is not necessary for the probe register.

4.3.3. Verification State Machine

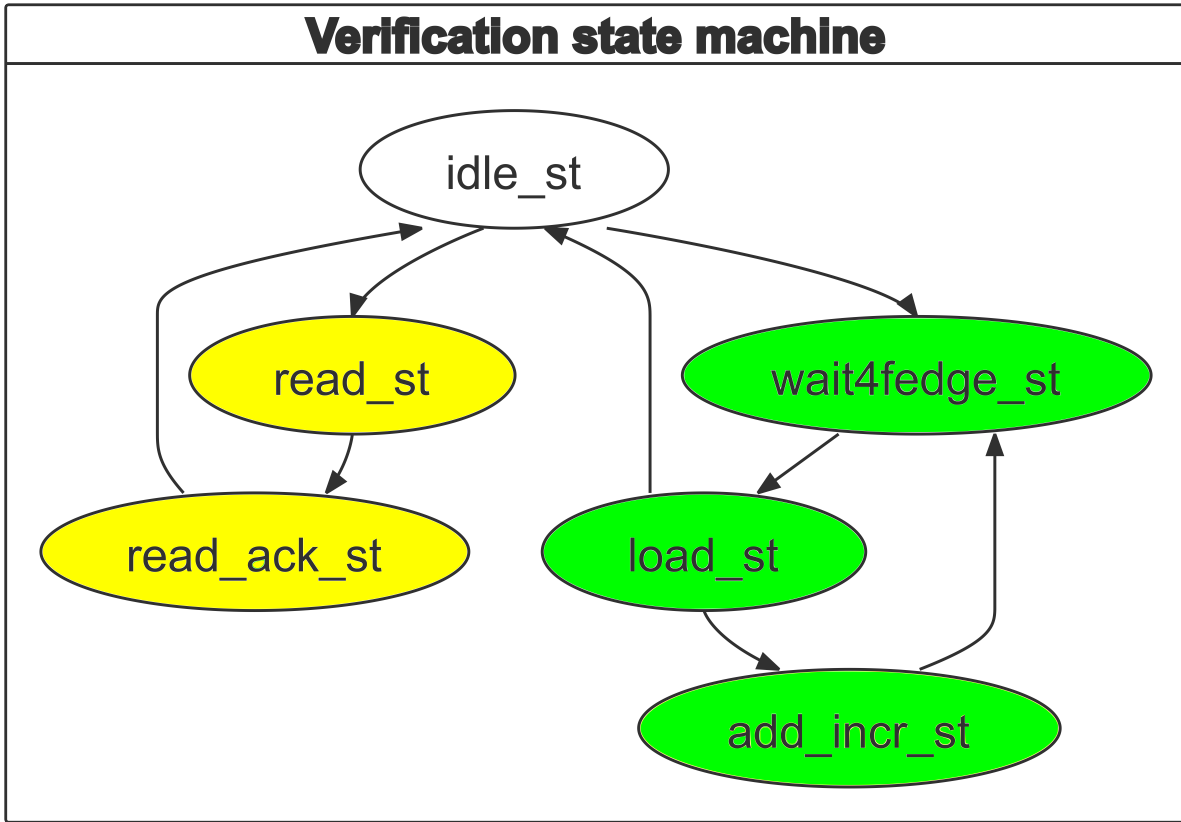


Figure 4.4.: Finite state machine for verifying the configuration of the Citiroc1A ASIC. States belonging to the same processes are represented with the same colour.

The Verification state machine, illustrated in Fig. 4.4 is responsible for verifying the configuration of the Citiroc1A ASIC. It is incorporated into the firmware, as shown in Fig. 4.1. It can be reset by the controlling computer by setting bit 2 of the status and control register to 1.

If bits are shifted into the serial register of the Citiroc1A ASIC, the **verification** process is automatically started. The **srou**t signal coming back from the ASIC, explained in section 3.3.2, is used to read back the shifted bits from the serial register of the Citiroc1A ASIC. The bits arrive at the FPGA in the same order as they were loaded in, but shifted by the length of the bitstream(1144/256). To compare the read back bits with the the loaded bits the bitstream has to be loaded twice.

The readback bits are stored in the verification RAM by the **verification** process and can be read by the controlling computer via the **read** process. This allows the controlling computer to compare the loaded bits with the read back bits and ensure that the configuration was loaded correctly into the serial register of the Citiroc1A ASIC.

4.4. The Provisional Readout

In addition to the configuration and verification of the configuration of Citroc1A ASIC, the firmware also provides a provisional readout in form of hit counters and time counters. The hit counters are used to count the number of hits on each channel of the Citroc1A ASIC.

They are limited to a minimal time between hits of two periods of the synchronization clock. In this case a 325 MHz clock is used, which corresponds to a minimal time between hits of 6.16 ns.

Each Citroc1A has 32 hit counters, one for each channel. The 32-bit hit counters are enabled by setting bit 6 of the status and control register of the corresponding Citroc1A Interface to 1. This also enables the time counter, which counts the number of clock cycles since it was last reset.

The hit counters and time counters are reset by setting bit 5 of the status and control register of the corresponding Citroc1A Interface to 1.

To read the hit and time counters, the controlling computer first has to disable the hit counters by setting bit 6 of the status and control register to 0, in order to avoid metastability issues arising from the clock domain crossing. The hit counters can then be read by the controlling computer via the IPBUS protocol.

The combination of the hit counters and the time counter allows the controlling computer to determine the number of hits per second on each channel of the Citroc1A ASIC.

4.5. Testing the Firmware

4.5.1. Setup for the Noise Measurement

The firmware will be evaluated through a noise measurement of the frontend electronics of the scintillating fiber hodoscope. The measurement will be performed with the SiPMs disconnected from the frontend electronics. The experimental setup is illustrated in Fig. 4.5.

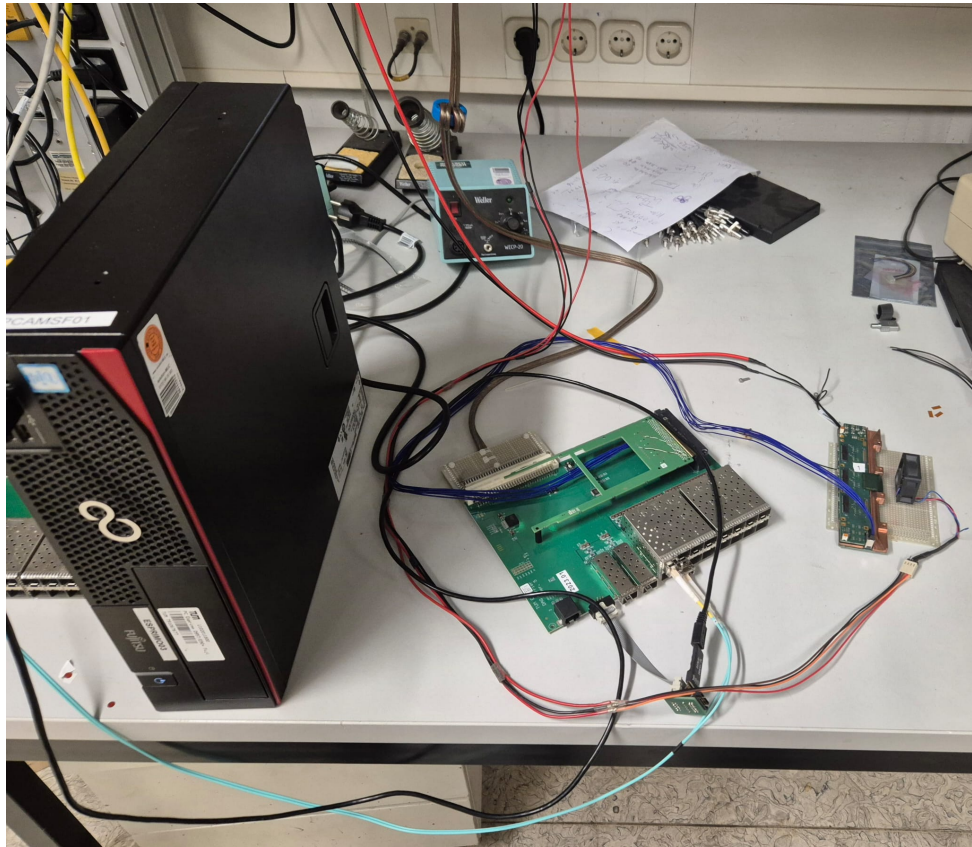


Figure 4.5.: Experimental setup for the noise measurement of the frontend electronics of the scintillating fiber hodoscope.

The measurement will be performed by the controlling computer, which will scan through a range of thresholds of the time discriminator of the Citiroc1A ASIC and record the number of hits per second on each channel with a measurement time of 400 ms. This scan will be performed for several different high gains near the maximum value of 62.

For comparison, the threshold scan will also be performed with the same configuration of the Citiroc1A ASICs on an Evaluation Board provided by Weeroc company, with the setup shown in Fig. 4.6.

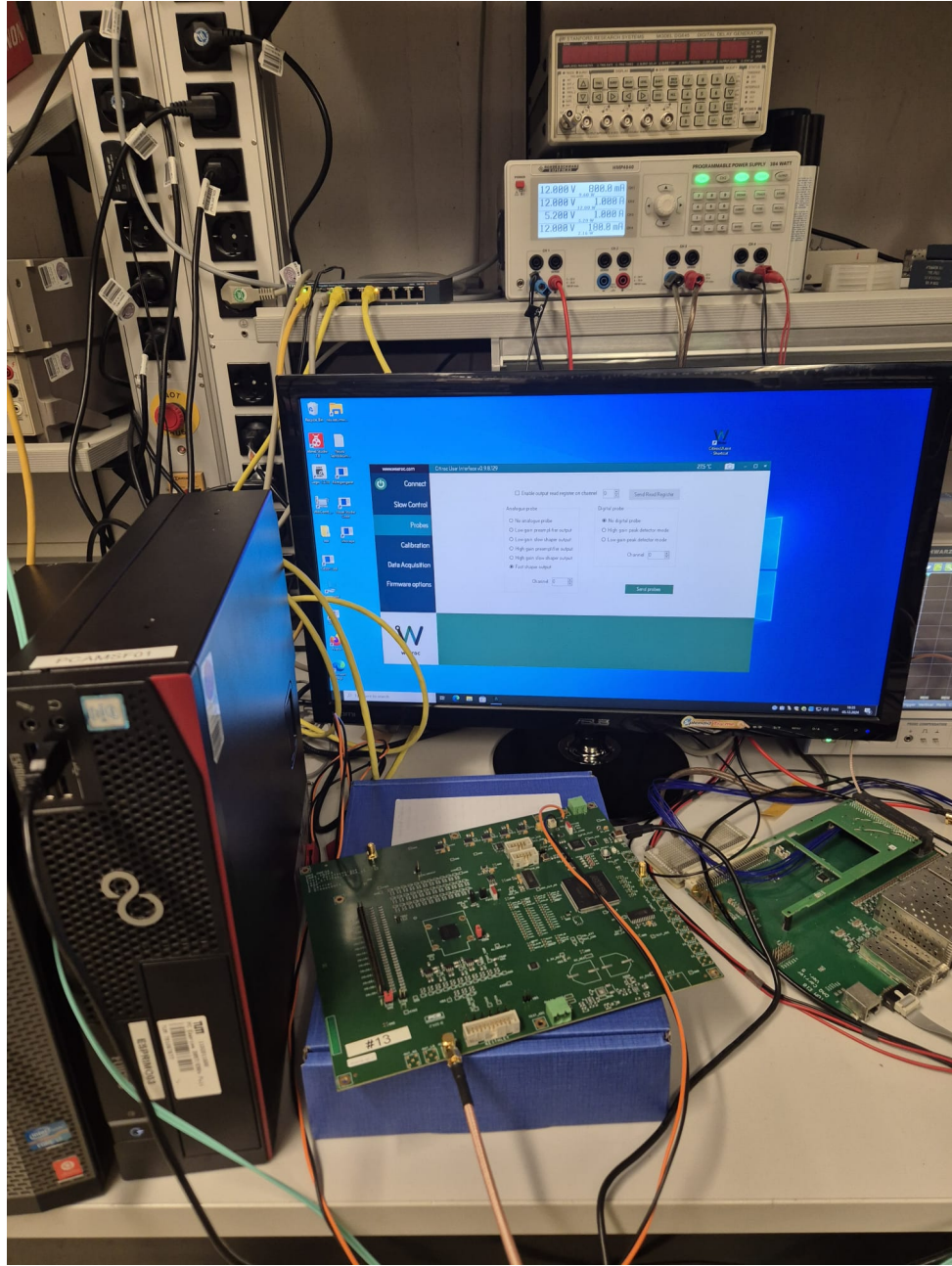


Figure 4.6.: Experimental setup for the noise measurement with an Evaluation Board provided by Weeroc company.

4.5.2. Theoretical Background for the Noise Measurement

The noise on the unconnected frontend electronics is assumed to be of gaussian distribution,

$$P(x) = \frac{1}{\sqrt{2\pi}\sigma} e^{-\frac{(x-\mu)^2}{2\sigma^2}} \quad (4.1)$$

where μ is the mean and σ the standard deviation of the noise[10].

The number of hits per second on each channel of the ASIC is proportional to the number of noise events above the threshold of the time discriminator but limited by the bandwidth of the fast shaper[10].

The number of hits per second vs. the threshold of the time discriminator is expected to follow an S-curve, which can be described by a modified error function,

$$N = \frac{A}{2} \left(1 - \operatorname{erf} \left(\frac{x - \mu}{\sqrt{2}\sigma} \right) \right) \quad (4.2)$$

where N is the number of hits per second, x the threshold of the time discriminator and A a renormalization factor[10].

CHAPTER 5

Measurement Results

5.1. Noise Measurements

For the noise measurement, the threshold was scanned in steps of 1 for a range of high gains, starting with a gain of 58 and ending with a maximal gain of 62.

The number of hits was measured for each of the 32 channels of the ASICs within a time interval of 400 ms. The threshold scan was performed for both the ASICs of FPGA 1 and 2.

The results of the threshold scan are shown for both ASICs of FPGA 1 and 2 for gains 58 to 62 in Figs. 5.1, 5.2, 5.3, 5.4 and 5.5 respectively.

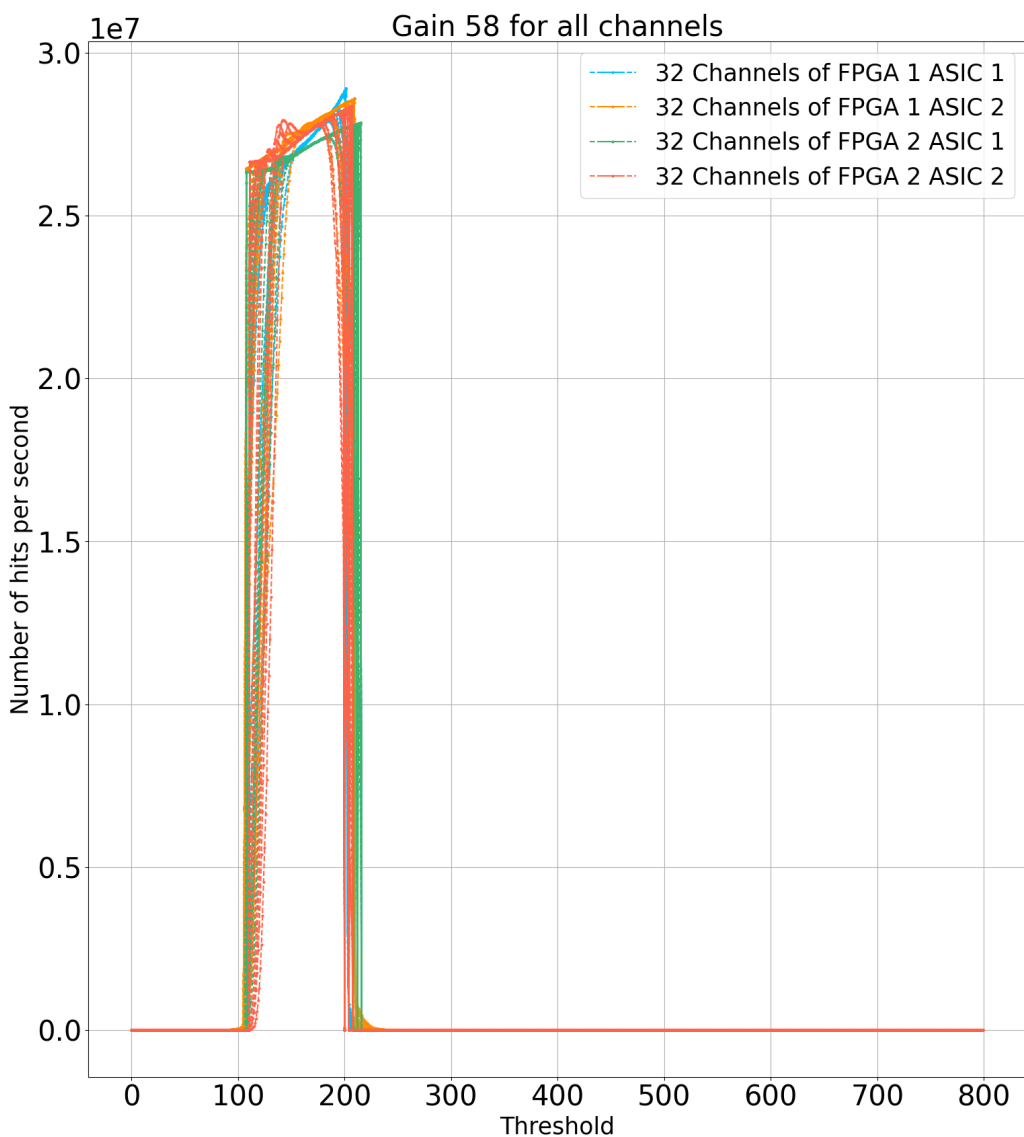


Figure 5.1.: Threshold scan of the Citiroc1A ASICs of FPGA 1 and 2 for gain 58 from threshold 0 to 800.

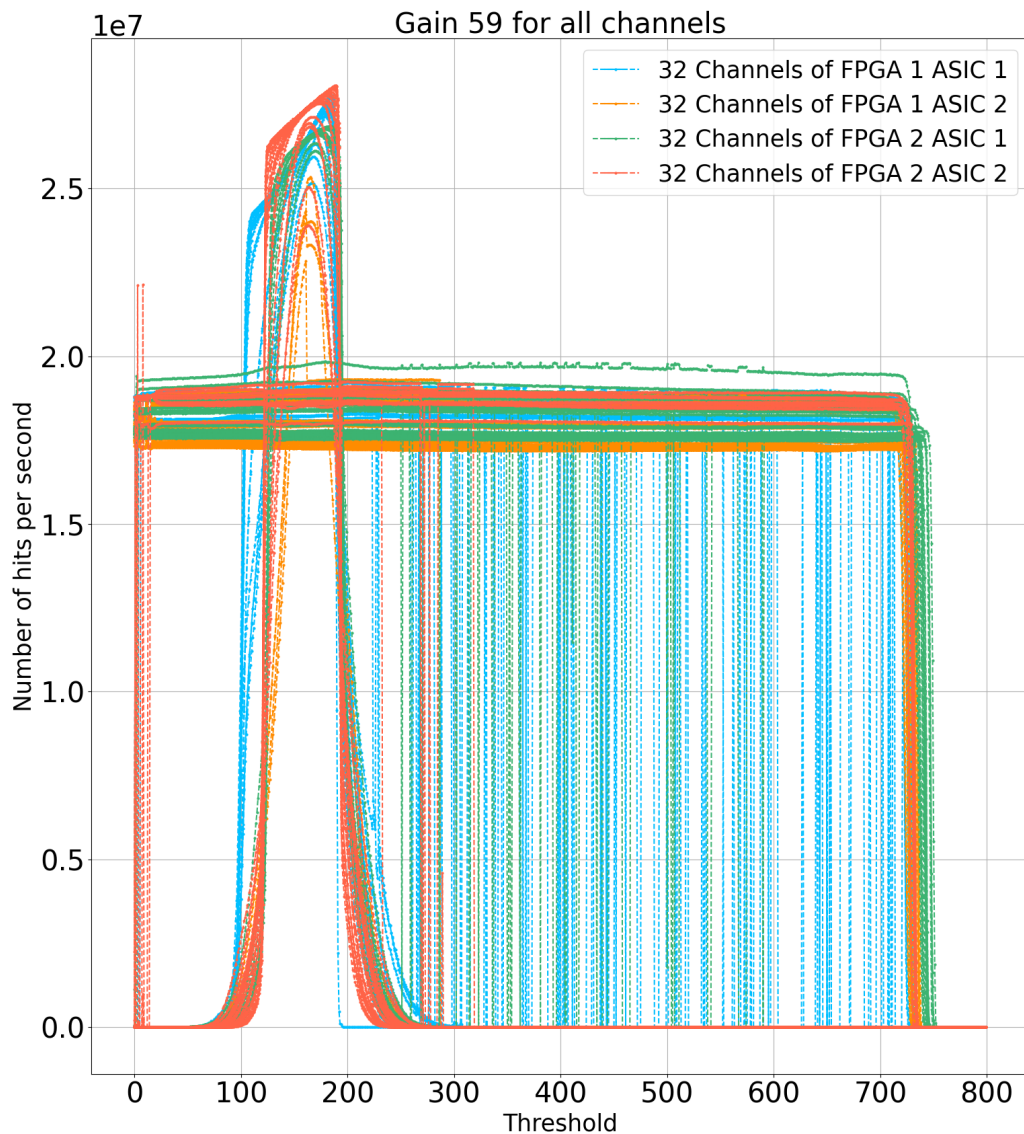


Figure 5.2.: Threshold scan of the Citiroc1A ASICs of FPGA 1 and 2 for gain 59 from threshold 0 to 800.

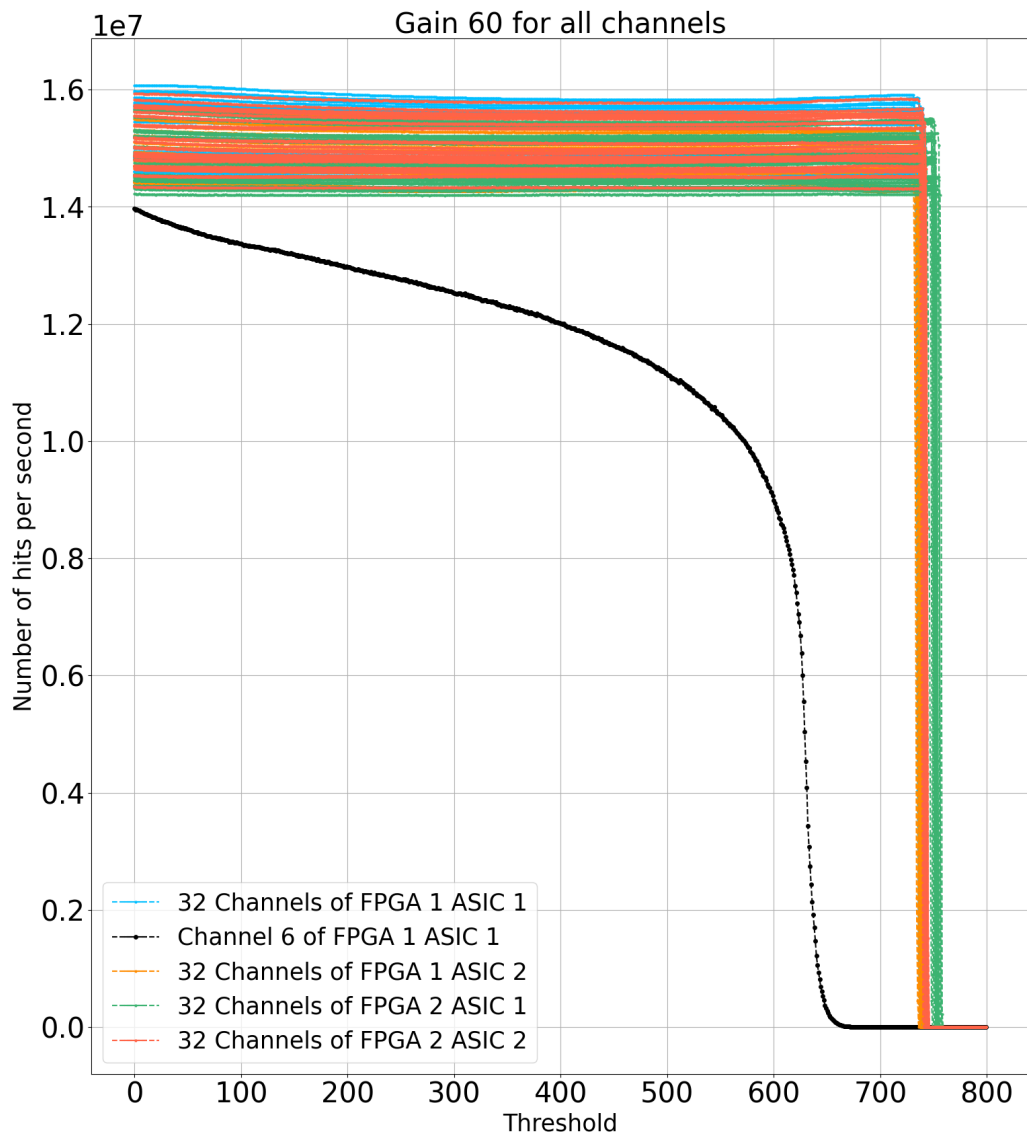


Figure 5.3.: Threshold scan of the Citiroc1A ASICs of FPGA 1 and 2 for gain 60 from threshold 0 to 800.

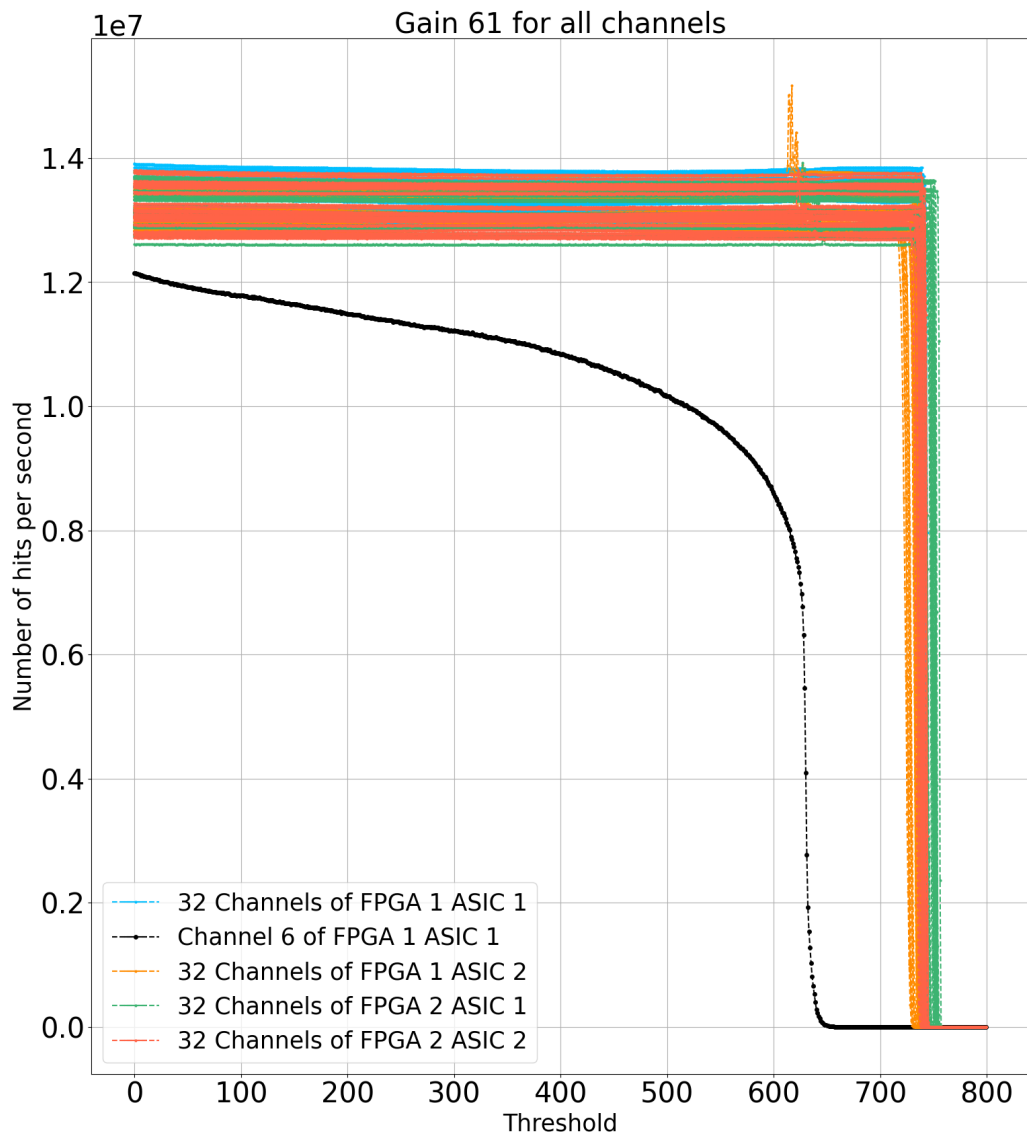


Figure 5.4.: Threshold scan of the Citiroc1A ASICs of FPGA 1 and 2 for gain 61 from threshold 0 to 800.

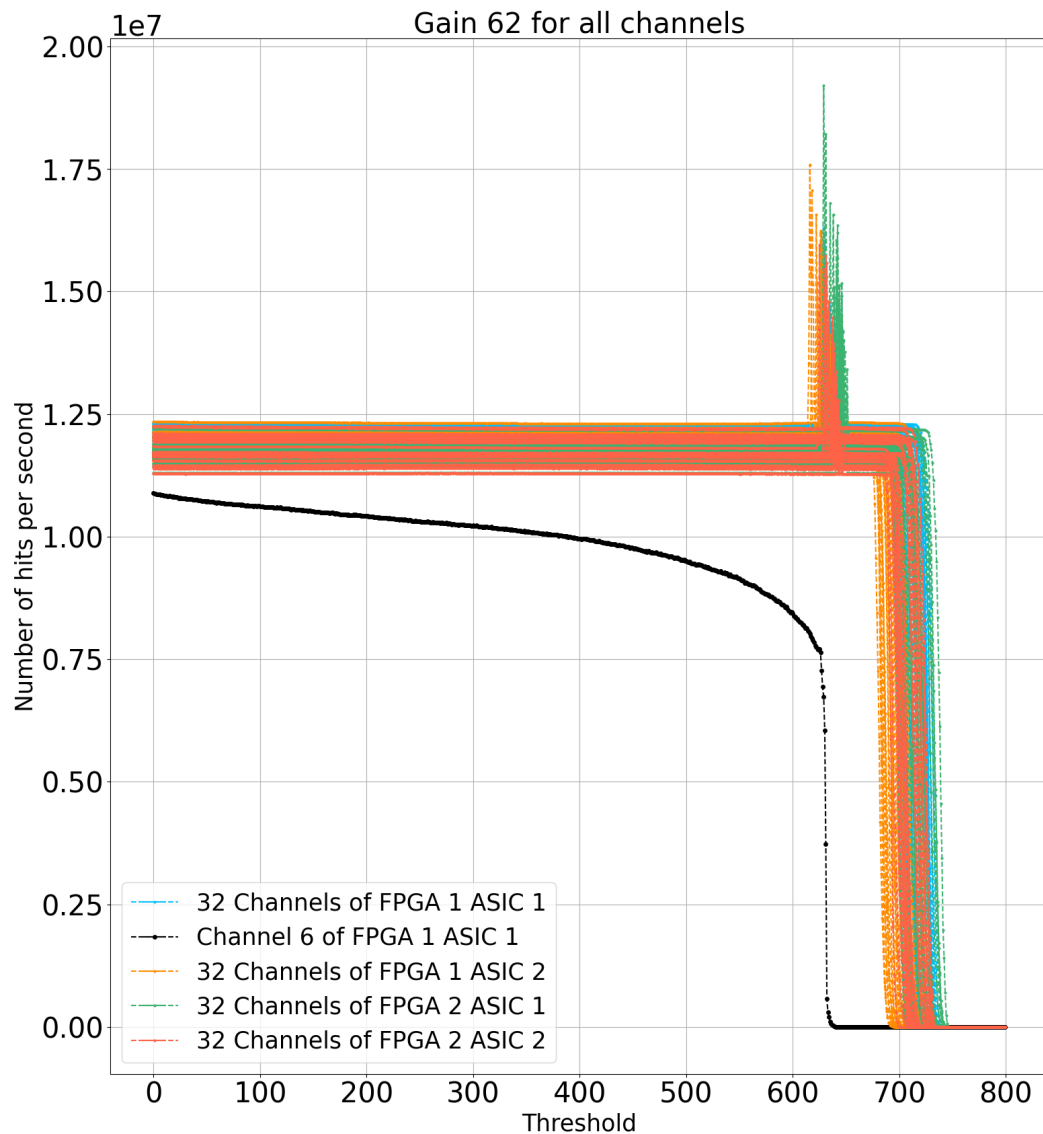


Figure 5.5.: Threshold scan of the Citiroc1A ASICs of FPGA 1 and 2 for gain 62 from threshold 0 to 800.

5.2. Frontend Electronics Characterization

5.2.1. Firmware Evaluation

Before performing the final noise measurements, I thoroughly verified the firmware functionality by performing the following tests:

-
- Using the internal probing capabilities of the Citiroc1A to verify the configuration of the ASICs, described in section 3.3.2.
 - Turning off individual channels of the ASICs by turning off the amplification of the channels or setting it to a low gain.
 - Disabling specific stages of the ASIC, such as the fast shaper or the time discriminator.
 - Using the output configuration of the Citiroc1A to turn off all triggers of the ASICs.

5.2.2. S-curve Analysis

In order to determine the optimal threshold and characterize the noise of the ASICs of FPGA 1 and 2, an S-curve analysis was performed.

The falling edge of the pedestal is fitted with the S-curve described in section 4.5.2

The results of the S-curve analysis are shown exemplarily for channel 0 of Citiroc1A 1 of FPGA 1 with gain 60,61 and 62 in Figs. 5.6, 5.7 and 5.8.

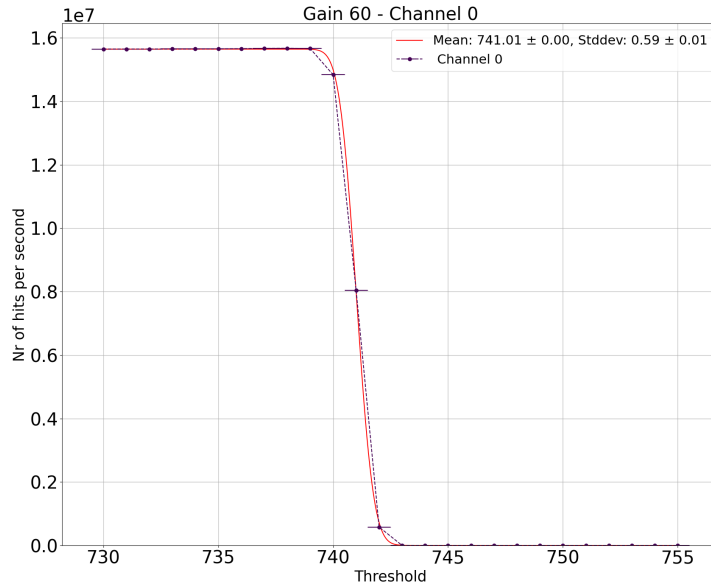


Figure 5.6.: Results of the S-curve analysis for channel 0 of Citiroc1A 1 of FPGA 1 with gain 60.

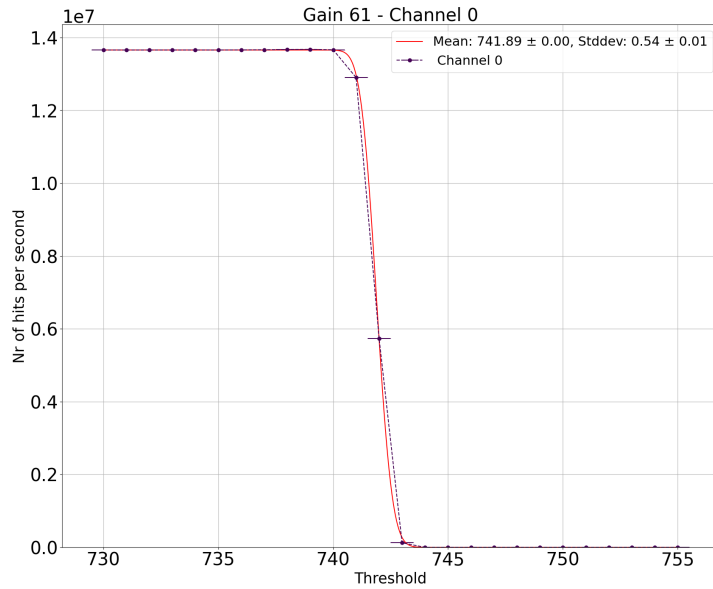


Figure 5.7.: Results of the S-curve analysis for channel 0 of Citiroc1A 1 of FPGA 1 with gain 61.

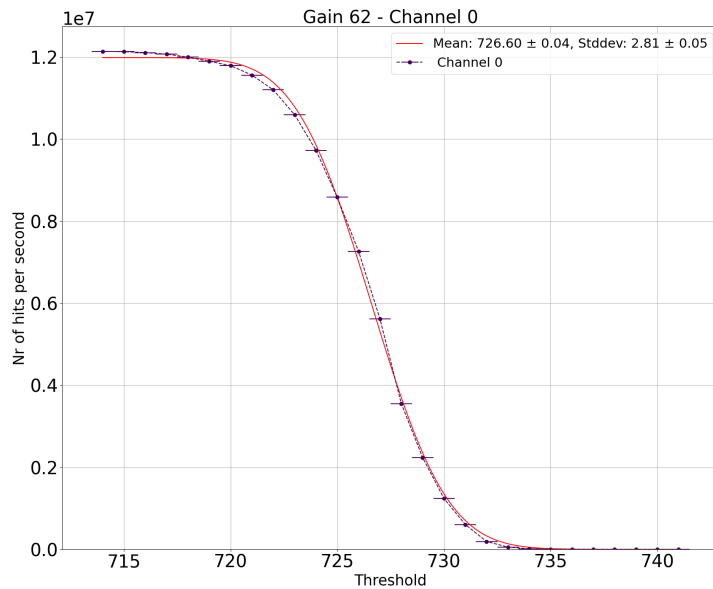


Figure 5.8.: Results of the S-curve analysis for channel 0 of Citiroc1A 1 of FPGA 1 with gain 62.

The S-curve fit, for all channels, for the high gain of 62 needed for the PRM experiment is shown in Fig. 5.9.

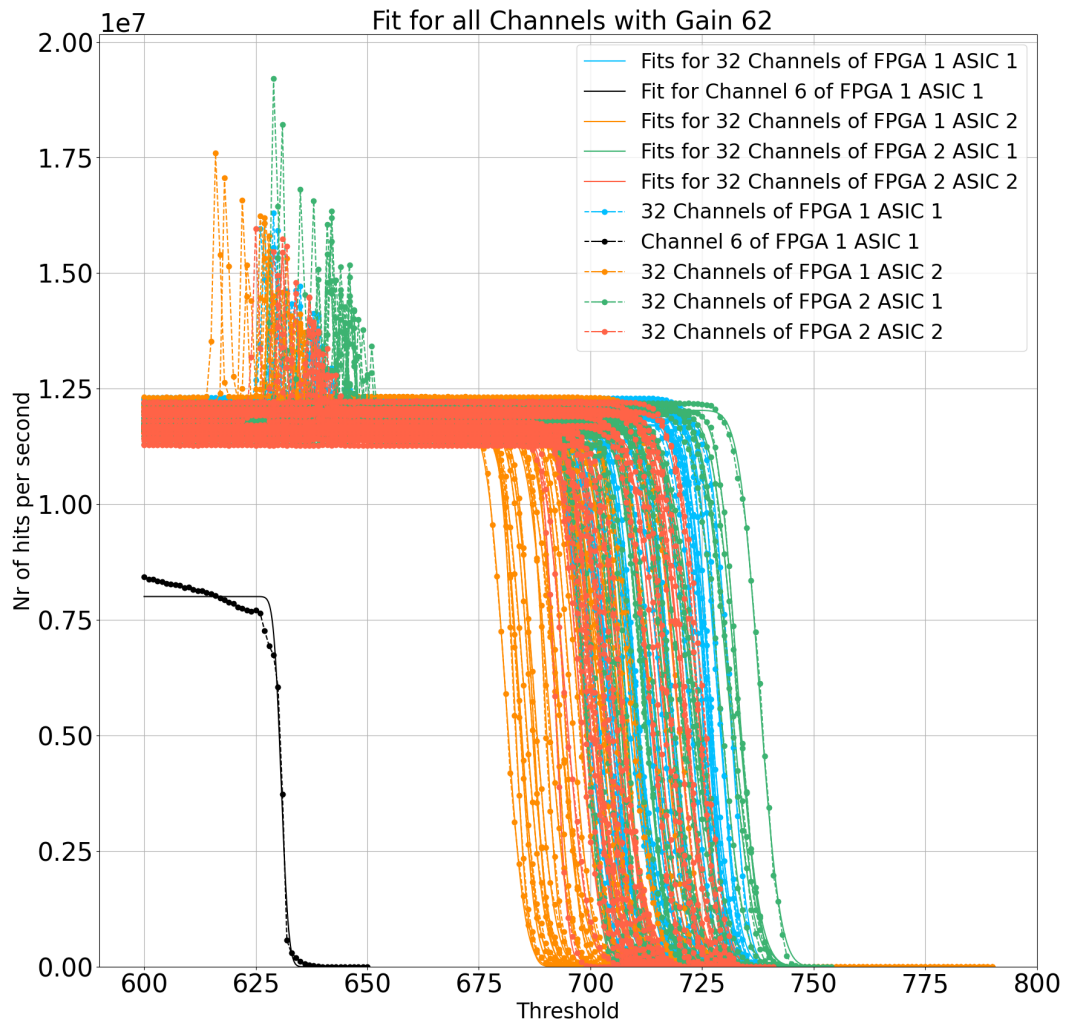


Figure 5.9.: Results of the S-curve analysis for all channels of the Citiroc1A ASICs of FPGA 1 and 2 with gain 62.

The mean μ and the standard deviation σ of the noise distribution were determined from the S-curve fits and are shown in Appendix B. They are plotted against the gain for all channels in Figure 5.10.

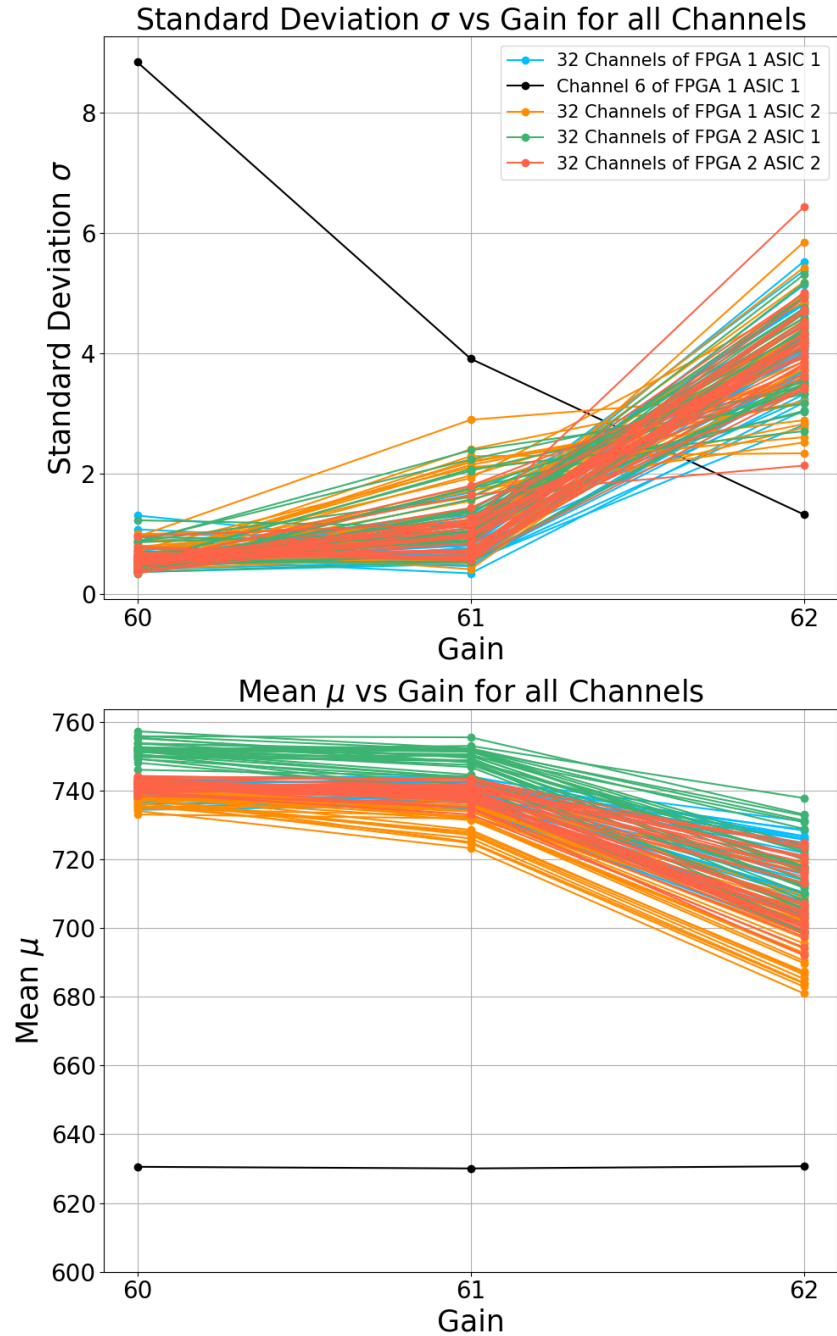


Figure 5.10.: Mean μ and standard deviation σ determined from the S-curve fits for all channels of the Citiroc1A ASICs of FPGA 1 and 2 plotted vs the gain.

5.2.3. Comparison with Evaluation Board

A comparison of the threshold scan to one performed with the same configuration of the Citiroc1A ASIC on a by Weeroc company provided Evaluation Board with gain 58 is shown in Fig. 5.11.

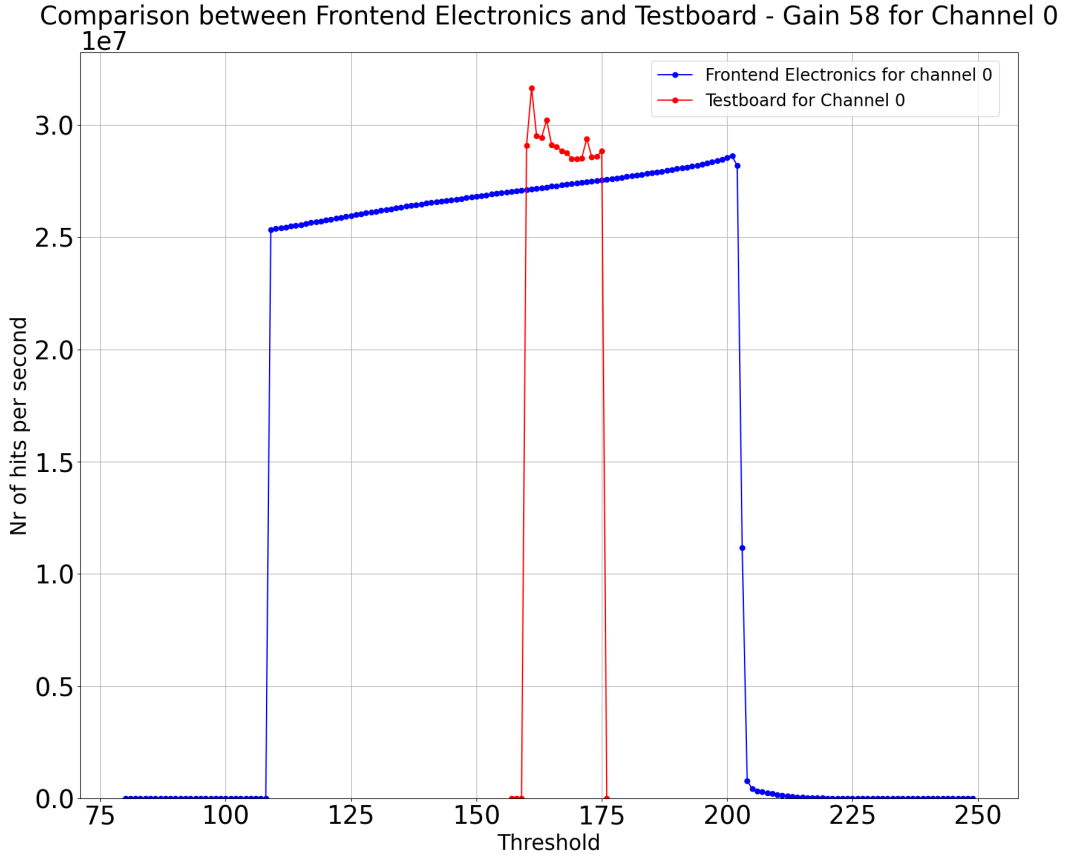


Figure 5.11.: Comparison of the threshold scan of the frontend electronics to the threshold scan performed on a by Weeroc company provided Evaluation Board with a gain of 58.

The pedestal of the threshold scan performed with the frontend electronics is far larger than the pedestal of the threshold scan performed with the Evaluation Board. This difference in the observed behaviour of the frontend electronics can currently not be explained.

5.2.4. Behaviour at different Gain Setting

The threshold scan of the Citiroc1A ASICs in the frontend electronics shows different behaviour for gain ranges of 0 to 58 (Figs. 5.1) and 60 to 62 (Figs. 5.3, 5.4 and 5.5), with the threshold scan at gain 59 showing a transition between the two behaviours depicted in Fig. 5.2. This difference is also currently not understood and is suspected to have the same cause as the difference in the threshold scan compared to the Evaluation Board measurement.

A general trend of the standard deviation σ of the S-curve increasing and the mean μ decreasing with higher gain is observed in Fig. 5.10.

5.2.5. Channel Behaviour Analysis

From the S-curve analysis it can be observed that the channels of the Citroc1A ASICs show different behaviour in the threshold scan.

Especially channel 6 of Citroc1A 1 of FPGA 1 shows a significantly different behaviour compared to the other channels, as can be seen in Fig. 5.10 and in the results of the threshold scan shown in Figs. 5.3, 5.4 and 5.5.

Furthermore, for the threshold scan with gain 59 depicted in Fig. 5.2 , all the channels show diverging behaviour, this is also suspected to be because of the transition between the two gain regions.

The behaviour of channel 6 of Citroc1A 1 of FPGA 1 seems to have a different cause than the gain transition and needs further investigation. This could be investigated by performing a threshold scan with another FEE PCB and comparing the results.

5.2.6. Summary of the Characterisation

The threshold scan and the S-curve analysis show that the frontend electronics of the SFH do not perform as expected. The noise behaviour at different gains is not consistent with the change of the gain value.

Due to this, a calibration of the individual channels of the frontend electronics is not yet possible. The cause of the observed behaviour is currently under investigation. The following sources are being considered:

- Ripple noise on the power supplies of the frontend electronics.
- Software error that causes the ASIC to be configured with a wrong configuration.
- Mistake in the circuit diagram or the layout of the PCBs.

Furthermore, the behaviour of channel 6 of Citroc1A 1 of FPGA 1 seems to have a different cause than the gain transition and also needs further investigation.

CHAPTER 6

Conclusion and Outlook

6.1. Personal Contribution

In this thesis, I developed the firmware and software, for the three FPGAs of the front-end electronics of the scintillating fiber hodoscope (SFH) responsible for the control and provisional readout of the Citroc1A ASICs.

For this, I structured the firmware hierarchically into different modules, responsible for the configuration of the Citroc1A ASICs, communication with the controlling computer and the readout of the ASICs and developed it in VHDL using Xilinx Vivado.

I tested the firmware and characterized the frontend electronics with a threshold scan and an S-curve analysis.

6.2. Conclusion

The threshold scan shows that the Citroc1A ASICs can be successfully configured but that the frontend electronics show abnormal behaviour. I conclude that the developed firmware allows for the configuration and provisional readout of the Citroc1A ASICs, but that the frontend electronics of the SFH is not performing as desired.

6.3. Outlook

The next steps in the development of the frontend electronics for the SFH are, the integration of this part of the firmware with the rest of the frontend electronics and the final

Chapter 6. Conclusion and Outlook

readout of the SFH. Moreover, additional investigation into the abnormal behaviour of the frontend electronics observed during the noise measurement is required.

This could be accomplished using the internal probing capabilities of the Citroc1A ASICs. Furthermore, tests with different FEE PCBs could be performed to investigate the origin of the observed behaviour.

By conducting these proposed steps and completing the development of the frontend electronics, the scintillating fiber hodoscope will be one step closer to being fully operational and performing its role in the PRM experiment and help solve the proton radius puzzle.

APPENDIX A

Configurable Registers of the Citiroc1A ASIC

Table A.1.: Configurable registers of the slow control register^[7]

Field	Bits	Default	Position	Description
Register:channel_thr_time				
ch_0	4	0	0	Channel-dependent 4-bit threshold for time discriminator.
:				
ch_31	4	0	-	-
Register:channel_thr_charge				
ch_0	4	0	128	Channel-dependent 4-bit threshold for charge discriminator.
:				
ch_31	4	0	-	-
Register:discriminator_power				
discriminator_charge_en	1	0	256	Enable charge discriminator.
discriminator_charge_pp	1	0	-	Power pulse for charge discriminator.
discriminator_latched_output	1	0	-	1: latched, 0: direct output.

Configurable registers of the slow control register continued on next page

Appendix A. Configurable Registers of the Citroc1A ASIC

Field	Bits	Default	Position	Description
discriminator_time_en	1	1	-	Enable time discriminator.
discriminator_time_pp	1	1	-	Power pulse for time discriminator.
4bit_dac_charge_en	1	0	261	Enable 4-bit charge DAC.
4bit_dac_charge_pp	1	0	-	Power pulse for 4-bit charge DAC.
4bit_dac_time_en	1	1	-	Enable 4-bit time DAC.
4bit_dac_time_pp	1	1	-	Power pulse for 4-bit time DAC.
ch_0	1	1	265	0: masked, 1: unmasked.
:				
ch_31	1	1	-	-
Register:track_and_hold_power				
high_gain_pp	1	0	297	Enable high gain.
high_gain_en	1	0	-	-
low_gain_pp	1	0	-	Power pulse for low gain.
low_gain_en	1	0	-	Enable low gain.
weak_bias	1	0	-	1: weak bias (600kHz max), 0: high bias (5MHz max).
Register:peak_detector_power				
high_gain_pp	1	0	302	Enable high gain for peak detector.
high_gain_en	1	0	-	-
low_gain_pp	1	0	-	Power pulse for low gain.
low_gain_en	1	0	-	Enable low gain for peak detector.
Register:select_peak_sensing				
high_gain_th	1	0	306	0: peak detector, 1: track and hold.
low_gain_th	1	0	-	-
peak_sensing_cell_bypass	1	0	-	0: cell active, 1: bypass peak sensing cell.
peak_sensing_external_trigger	1	0	-	0: internal trigger, 1: external trigger.

Configurable registers of the slow control register continued on next page

Field	Bits	Default	Position	Description
Register:shaper				
fast_shaper_follower_pp	1	0	310	Power pulse for fast shaper follower.
fast_shaper_en	1	1	-	Enable fast shaper.
fast_shaper_pp	1	1	-	Power pulse for fast shaper.
low_gain_slow_shaper_pp	1	0	-	Power pulse for low gain slow shaper.
low_gain_slow_shaper_en	1	0	-	Enable low gain slow shaper.
low_gain_slow_shaper_time_const	3	0	-	See the table above for values.
high_gain_slow_shaper_pp	1	0	-	Power pulse for high gain slow shaper.
high_gain_slow_shaper_en	1	0	-	Enable high gain slow shaper.
high_gain_slow_shaper_time_const	3	0	-	See the table above for values.
Register:pre_amp_power				
low_gain_weak_bias	1	0	323	0: normal bias, 1: weak bias.
high_gain_pp	1	1	-	Power pulse for high gain preamp.
high_gain_en	1	1	-	Enable high gain preamp.
low_gain_pp	1	0	-	Power pulse for low gain preamp.
low_gain_en	1	0	-	Enable low gain preamp.
fast_shaper_low_gain	1	0	-	0: fast shaper on high gain.
Register:input_dac				
dac_en	1	1	329	Input DAC for bias correction.
dac_ref	1	1	-	Voltage ref: 1 = internal 4.5V, 0 = internal 2.5V, depends on vdd_dac.

Configurable registers of the slow control register continued on next page

Appendix A. Configurable Registers of the Citiroc1A ASIC

Field	Bits	Default	Position	Description
ch_0	8	255	-	VSipm = V_HV - V_DAC (check what makes sense here).
ch_0_en	1	1	-	Enable channel 0 input DAC.
:				
ch_31	8	255	-	Same as ch_0 for channel 31.
ch_31_en	1	1	-	Enable channel 31 input DAC.
Register:channel_preamp				
ch_0_hg	6	62	619	High gain preamp setting.
ch_0_lg	6	0	-	Low gain preamp setting.
ch_0_ctest_hg	1	0	-	1: Connect injection capacitance for test signal.
ch_0_ctest_lg	1	0	-	1: Connect low gain injection capacitance.
ch_0_disable	1	0	-	1 disables preamp for channel 0.
:				
ch_31_hg	6	62	-	High gain preamp setting.
ch_31_lg	6	0	-	Low gain preamp setting.
ch_31_ctest_hg	1	0	-	1: Connect injection capacitance for test signal.
ch_31_ctest_lg	1	0	-	1: Connect low gain injection capacitance.
ch_31_disable	1	0	-	1 disables preamp for channel 0.
Register:service_blocks				
temp_pp	1	1	999	Enable power pulse for temperature monitoring.
temp_en	1	1	-	Enable temperature monitoring.
band_gap_pp	1	1	-	Enable power pulse for band gap reference.

Configurable registers of the slow control register continued on next page

Field	Bits	Default	Position	Description
band_gap_en	1	1	-	Enable band gap reference.
Register:threshold_dac				
charge_dac_en	1	0	1103	Enable charge threshold DAC.
charge_dac_pp	1	0	-	Power pulse for charge threshold DAC.
time_dac_en	1	1	-	Enable time threshold DAC.
time_dac_pp	1	1	-	Power pulse for time threshold DAC.
charge_threshold	10	0	-	Charge threshold value.
time_threshold	10	-	-	Time threshold value (e.g., 200 for 1 cell min, 250 for 2 cells).
Register:otaq_power				
high_gain_en	1	1	1127	Enable high gain for OTAQ.
high_gain_pp	1	1	-	Power pulse for high gain OTAQ.
low_gain_en	1	0	-	Enable low gain for OTAQ.
low_gain_pp	1	0	-	Power pulse for low gain OTAQ.
debug_probe_en	1	1	-	Enable debug probe.
debug_probe_pp	1	1	-	Power pulse for debug probe.
Register:input_output				
output_buffer_bias	1	0	1133	Output OTA buffer bias: 0 = auto bias, 1 = force on.
val_event_receiver_en	1	1	-	Enable validation event receiver.
val_event_receiver_pp	1	1	-	Power pulse for validation event receiver.
raz_chn_en	1	1	-	Enable RAZ channel.
raz_chn_pp	1	1	-	Power pulse for RAZ channel.

Configurable registers of the slow control register continued on next page

Appendix A. Configurable Registers of the Citiroc1A ASIC

Field	Bits	Default	Position	Description
digital_output_en	1	1	-	Enable digital multiplexed output.
or32_output_en	1	1	-	Enable OR32 output.
or32_oc_output_en	1	1	-	Enable OR32 over-current output.
trigger_polarity	1	0	-	Trigger polarity: 0 = positive (rising edge), 1 = negative (falling edge).
or32_t_oc_en	1	1	-	Enable OR32 timeout over-current.
32_triggers_en	1	1	1143	Enable 32 triggers.

Table A.2.: Configurable registers of the probe register[7]

Register	Field	Bits	Position	Type
out_probe_fast_shaper	ch_0 ⋮ ch_31	1 ⋮ 1	0 ⋮ 31	Analog - Out_probe
out_probe_slow_shaper_lg	ch_0 ⋮ ch_31	1 ⋮ 1	32 ⋮ 63	Analog - Out_probe
digital_probe_peak_sense_lg	ch_0 ⋮ ch_31	1 ⋮ 1	64 ⋮ 95	Digital - Digital_probe
out_probe_slow_shaper_hg	ch_0 ⋮ ch_31	1 ⋮ 1	96 ⋮ 127	Analog - Out_probe
digital_probe_peak_sense_hg	ch_0 ⋮ ch_31	1 ⋮ 1	128 ⋮ 159	Digital - Digital_probe
out_probe_preamp_hg	ch_0 ⋮ ch_31	1 ⋮ 1	160 ⋮ 191	Analog - Out_probe
out_probe_preamp_lg	ch_0 ⋮ ch_31	1 ⋮ 1	192 ⋮ 223	Analog - Out_probe
input_dac_probe	ch_0 ⋮ ch_31	1 ⋮ 1	224 ⋮ 255	Analog - Out_probe_dac_5V

APPENDIX B

Fit Parameters of the S-Curve Analysis

Gain	Channel	μ of C1 F1	σ of C1 F1	μ of C2 F1	σ of C2 F1	μ of C1 F2	σ of C1 F2	μ of C2 F2	σ of C2 F2
58	ch_0	202.00	0.60	209.59	0.05	215.71	0.06	207.77	0.06
	ch_1	202.00	0.60	209.83	0.07	215.71	0.06	207.76	0.06
	ch_2	202.01	0.61	209.76	0.08	210.68	5.50	207.76	0.06
	ch_3	202.00	0.60	209.75	0.08	211.28	5.46	207.76	0.06
	ch_4	202.01	0.61	209.29	0.20	215.61	0.08	204.03	4.72
	ch_5	202.00	0.61	209.73	0.09	215.79	0.06	207.76	0.06
	ch_6	201.95	0.48	209.79	0.07	215.68	0.08	207.76	0.06
	ch_7	202.00	0.62	209.33	0.19	215.79	0.06	205.11	4.59
	ch_8	202.02	0.62	209.78	0.08	208.09	6.26	207.77	0.06
	ch_9	201.88	0.76	209.80	0.07	215.66	0.09	207.76	0.06
	ch_10	202.01	0.61	209.74	0.09	215.37	0.17	207.76	0.06
	ch_11	201.78	0.87	209.73	0.09	215.67	0.09	207.77	0.06
	ch_12	202.02	0.63	207.83	2.42	215.66	0.09	199.08	5.04
	ch_13	202.02	0.66	208.52	1.73	215.82	0.04	200.69	4.97
	ch_14	202.01	0.61	209.77	0.08	215.71	0.08	207.76	0.06
	ch_15	201.65	1.20	209.37	0.21	215.68	0.08	207.87	0.03
	ch_16	202.00	0.60	209.79	0.10	215.67	0.08	207.76	0.06
	ch_17	202.01	0.61	209.83	0.08	208.97	5.96	207.77	0.06
	ch_18	202.01	0.62	209.82	0.07	215.71	0.09	207.77	0.06
	ch_19	202.02	0.65	209.83	0.07	215.71	0.06	207.77	0.06
	ch_20	201.93	0.73	209.41	0.20	209.18	6.06	207.69	0.08
	ch_21	202.01	0.61	209.48	0.20	215.76	0.06	207.70	0.07
	ch_22	201.89	0.77	207.98	2.39	215.70	0.09	198.81	5.24
	ch_23	202.01	0.61	209.78	0.10	215.71	0.06	207.77	0.06
	ch_24	202.01	0.62	209.81	0.10	215.50	0.00	207.77	0.06
	ch_25	202.01	0.61	209.58	0.22	215.71	0.06	207.76	0.07
	ch_26	202.01	0.63	209.86	0.06	215.90	0.03	207.77	0.06
	ch_27	202.01	0.61	209.82	0.07	215.71	0.08	207.71	0.09
	ch_28	202.01	0.62	209.73	0.09	215.67	0.08	207.76	0.06
	ch_29	202.02	0.62	208.87	1.27	215.71	0.06	201.26	5.41
	ch_30	202.01	0.61	209.80	0.08	215.71	0.08	207.70	0.08
	ch_31	202.04	0.66	209.36	0.35	215.73	0.07	202.52	5.44

Table B.1.: Mean μ and standard deviation σ of the noise distribution gained from the fit of S-curve for gain 58.

Appendix B. Fit Parameters of the S-Curve Analysis

Gain	Channel	μ of C1 F1	σ of C1 F1	μ of C2 F1	σ of C2 F1	μ of C1 F2	σ of C1 F2	μ of C2 F2	σ of C2 F2
59	ch_0	196.32	9.86	286.45	0.14	196.76	6.06	192.84	3.08
	ch_1	196.03	9.26	731.10	1.85	193.94	14.47	194.52	3.94
	ch_2	195.05	8.02	722.27	3.14	260.12	3.10	193.59	1.78
	ch_3	192.94	20.01	174.42	30.04	734.90	3.12	194.29	3.28
	ch_4	197.16	11.26	722.99	2.58	197.46	7.03	191.72	5.85
	ch_5	192.13	21.02	730.69	1.83	741.43	1.99	193.63	3.68
	ch_6	189.46	1.27	724.90	2.67	739.22	2.39	194.28	3.66
	ch_7	729.57	1.82	724.84	2.60	746.93	1.77	192.11	8.38
	ch_8	727.35	1.79	727.13	2.09	741.23	1.66	NAN	NAN
	ch_9	729.81	1.82	731.51	1.81	742.72	1.59	194.91	6.82
	ch_10	263.61	6.57	199.37	17.71	747.08	1.45	193.87	2.34
	ch_11	229.80	0.25	725.48	2.44	745.86	1.50	195.06	5.87
	ch_12	728.83	1.09	729.47	1.65	741.21	1.81	730.21	1.78
	ch_13	726.97	1.10	728.01	1.60	194.60	11.81	186.52	18.82
	ch_14	730.18	1.00	196.86	18.67	739.68	3.27	193.76	1.92
	ch_15	731.62	1.05	731.88	1.58	742.00	1.69	268.74	0.09
	ch_16	730.12	2.8	731.34	1.29	188.54	25.05	194.89	7.43
	ch_17	297.72	0.10	726.70	1.71	746.58	1.49	195.17	7.70
	ch_18	225.17	4.88	734.32	1.00	743.01	1.31	194.84	10.03
	ch_19	1920.89	204.93	732.88	1.02	197.00	8.90	726.84	2.15
	ch_20	202.41	11.16	730.04	1.73	737.53	1.87	731.45	1.52
	ch_21	724.77	1.59	731.85	1.47	193.33	14.32	190.32	12.80
	ch_22	174.88	33.74	730.34	1.09	749.33	1.37	730.83	1.75
	ch_23	185.25	21.86	734.84	0.94	196.37	12.73	232.74	0.22
	ch_24	187.55	15.23	732.42	1.12	740.63	2.39	729.67	2.21
	ch_25	194.71	8.93	733.04	0.89	196.11	7.34	731.96	0.86
	ch_26	189.10	12.70	729.33	1.76	736.03	3.03	194.91	5.42
	ch_27	197.30	10.92	735.99	0.98	740.27	2.40	732.01	1.74
	ch_28	192.47	7.79	724.77	2.47	189.68	17.66	195.04	6.91
	ch_29	192.86	6.69	735.02	1.11	197.14	6.10	181.79	29.53
	ch_30	192.85	6.05	728.13	1.48	741.47	2.17	729.51	1.61
	ch_31	193.90	7.29	735.61	0.83	737.23	3.25	726.48	2.24

Table B.2.: Mean μ and standard deviation σ of the noise distribution gained from the fit of S-curve for gain 59.

Gain	Channel	μ of C1 F1	σ of C1 F1	μ of C2 F1	σ of C2 F1	μ of C1 F2	σ of C1 F2	μ of C2 F2	σ of C2 F2
60	ch_0	741.01	0.59	739.59	0.50	752.26	0.51	741.58	0.65
	ch_1	736.09	1.07	742.14	0.41	751.30	0.42	743.27	0.65
	ch_2	741.64	0.60	737.67	0.60	752.57	0.45	739.84	0.69
	ch_3	743.83	0.37	733.06	0.99	749.16	0.55	741.91	0.65
	ch_4	741.69	0.55	737.72	0.49	752.06	0.52	741.33	0.65
	ch_5	740.05	0.50	742.25	0.40	751.68	0.41	744.02	0.63
	ch_6	630.55	8.83	737.48	0.57	750.47	0.87	744.07	0.62
	ch_7	742.59	0.42	738.36	0.76	755.89	0.43	740.46	0.58
	ch_8	741.22	0.52	738.13	0.79	749.29	0.50	741.97	0.54
	ch_9	742.63	0.42	740.39	0.50	751.86	0.40	740.63	0.63
	ch_10	738.61	0.72	734.75	0.97	755.47	0.34	741.00	0.75
	ch_11	742.15	0.42	738.39	0.90	753.68	0.55	741.95	0.60
	ch_12	740.38	0.54	738.74	0.72	750.23	0.88	743.13	0.59
	ch_13	738.95	0.54	736.30	0.50	749.76	0.69	739.40	0.42
	ch_14	741.24	0.48	735.27	0.81	755.80	0.37	739.42	0.79
	ch_15	742.41	0.41	740.24	0.46	751.31	0.39	741.93	0.51
	ch_16	739.07	0.61	737.30	0.54	751.89	0.49	740.65	0.60
	ch_17	741.32	0.52	734.09	0.95	755.20	0.34	742.07	0.49
	ch_18	738.03	0.74	740.65	0.50	750.67	0.86	742.04	0.49
	ch_19	738.09	0.62	738.94	0.73	746.05	1.23	739.39	0.49
	ch_20	742.36	0.45	738.02	0.62	748.09	0.53	743.13	0.59
	ch_21	739.32	0.56	739.92	0.43	750.13	0.86	744.28	0.57
	ch_22	743.03	0.41	736.52	0.48	757.25	0.35	743.35	0.62
	ch_23	736.70	0.87	740.73	0.48	752.25	0.53	742.45	0.35
	ch_24	741.00	0.59	737.67	0.54	752.68	0.43	742.34	0.36
	ch_25	739.79	0.68	737.79	0.51	751.27	0.46	741.47	0.54
	ch_26	741.13	0.62	742.20	0.41	751.58	0.36	740.17	0.60
	ch_27	742.28	0.51	742.30	0.41	752.36	0.51	743.06	0.58
	ch_28	734.40	0.99	737.42	0.55	753.74	0.62	738.47	0.96
	ch_29	738.77	0.80	742.67	0.40	749.86	0.94	743.65	0.65
	ch_30	734.99	1.30	735.74	0.58	753.72	0.56	742.27	0.37
	ch_31	739.13	0.72	741.40	0.52	752.53	0.52	740.73	0.48

Table B.3.: Mean μ and standard deviation σ of the noise distribution gained from the fit of S-curve for gain 60.

Gain	Channel	μ of C1 F1	σ of C1 F1	μ of C2 F1	σ of C2 F1	μ of C1 F2	σ of C1 F2	μ of C2 F2	σ of C2 F2
61	ch.0	741.89	0.54	738.00	0.74	752.27	0.63	741.17	0.61
	ch.1	736.98	0.81	739.01	0.94	747.48	1.24	743.65	0.63
	ch.2	743.54	0.34	735.73	0.59	750.14	1.18	740.94	0.56
	ch.3	744.12	0.50	731.88	1.15	743.42	1.15	741.58	0.69
	ch.4	740.94	0.73	735.50	0.56	752.99	0.54	741.33	0.60
	ch.5	739.06	0.67	739.61	1.10	744.60	1.57	743.23	0.73
	ch.6	630.07	3.91	734.19	1.16	743.82	1.62	743.47	0.71
	ch.7	740.10	0.76	735.16	0.98	751.80	1.04	740.21	0.65
	ch.8	739.22	0.81	733.91	1.20	739.11	2.08	738.07	1.14
	ch.9	740.11	0.77	734.10	1.55	746.84	1.35	738.18	0.96
	ch.10	735.83	1.22	732.65	1.17	748.15	1.75	741.68	0.61
	ch.11	739.75	0.72	735.52	0.86	748.37	1.42	740.75	0.73
	ch.12	735.15	1.69	732.21	1.61	741.51	2.24	739.72	0.94
	ch.13	734.33	1.39	728.04	1.79	748.57	0.90	734.98	1.29
	ch.14	737.54	1.10	735.53	0.41	755.50	0.54	740.69	0.58
	ch.15	738.24	1.04	735.59	0.98	743.70	1.76	739.18	0.94
	ch.16	737.34	0.97	727.06	2.41	750.54	0.99	737.11	1.22
	ch.17	739.04	0.83	723.25	2.89	749.48	1.38	739.96	0.84
	ch.18	735.31	1.31	732.13	1.72	739.44	2.39	737.26	1.43
	ch.19	734.49	1.24	728.58	2.11	744.19	1.11	733.06	1.80
	ch.20	740.60	0.71	731.41	1.93	739.78	2.05	738.54	1.16
	ch.21	736.88	1.02	734.99	1.22	748.81	1.04	742.61	0.73
	ch.22	742.28	0.56	724.72	2.29	752.30	1.40	738.79	0.96
	ch.23	734.51	1.17	732.30	1.97	751.88	0.72	738.53	1.01
	ch.24	741.52	0.64	727.46	2.14	750.05	1.15	737.67	1.24
	ch.25	740.97	0.56	725.03	2.22	751.89	0.65	734.94	1.65
	ch.26	742.49	0.46	740.97	0.63	748.70	1.06	739.20	0.71
	ch.27	742.76	0.55	733.96	1.41	748.30	1.29	739.11	1.09
	ch.28	735.76	0.95	735.34	0.51	751.35	1.04	736.48	1.17
	ch.29	740.07	0.54	736.37	1.15	750.14	0.87	741.53	0.83
	ch.30	737.72	0.75	726.08	2.19	751.84	0.89	738.74	1.09
	ch.31	740.97	0.53	731.70	1.72	751.26	0.87	737.39	1.18

Table B.4.: Mean μ and standard deviation σ of the noise distribution gained from the fit of S-curve for gain 61.

Gain	Channel	μ of C1 F1	σ of C1 F1	μ of C2 F1	σ of C2 F1	μ of C1 F2	σ of C1 F2	μ of C2 F2	σ of C2 F2
62	ch.0	726.60	2.81	713.25	4.66	731.30	4.69	717.16	4.33
	ch.1	718.02	3.99	707.30	3.73	714.10	4.74	723.34	4.69
	ch.2	731.05	3.18	708.57	4.55	717.47	4.59	723.90	3.40
	ch.3	726.76	3.74	705.94	5.43	705.84	3.38	720.48	4.91
	ch.4	715.61	4.29	706.72	4.42	737.82	3.61	719.20	4.18
	ch.5	712.48	4.39	709.42	4.45	706.49	3.04	717.28	4.72
	ch.6	630.71	1.32	701.70	4.33	705.45	4.07	720.55	4.24
	ch.7	710.35	3.72	702.83	4.98	717.67	3.47	716.01	5.01
	ch.8	709.68	4.66	698.26	4.24	698.83	2.71	702.71	3.86
	ch.9	710.21	4.28	695.52	3.73	710.03	4.36	705.11	4.53
	ch.10	703.89	4.81	702.32	5.19	708.00	3.02	721.05	3.82
	ch.11	709.77	3.65	701.87	5.85	711.97	4.17	713.00	4.49
	ch.12	698.74	4.06	692.80	3.86	701.20	3.44	704.06	4.14
	ch.13	699.15	4.58	687.40	3.57	722.67	4.92	697.49	3.66
	ch.14	704.50	4.48	718.96	4.38	733.07	3.57	724.83	4.10
	ch.15	704.16	3.94	700.24	4.55	703.29	3.53	706.64	4.31
	ch.16	710.07	5.13	685.21	3.51	722.10	4.75	703.03	3.60
	ch.17	709.08	4.47	680.97	3.33	712.25	3.49	706.71	4.73
	ch.18	703.11	4.83	692.07	2.82	698.94	3.16	698.39	3.95
	ch.19	701.14	5.37	686.94	2.60	712.96	4.94	694.37	3.92
	ch.20	713.91	4.22	692.56	4.84	698.83	3.32	700.33	3.77
	ch.21	707.81	5.52	697.01	4.25	720.14	5.30	714.82	4.18
	ch.22	721.86	4.10	682.96	2.34	716.58	4.25	700.42	3.41
	ch.23	703.91	4.86	690.54	3.62	728.87	4.13	700.98	4.24
	ch.24	723.89	4.06	686.47	3.20	718.08	4.52	699.47	4.45
	ch.25	725.72	3.50	683.87	2.89	732.71	4.13	692.14	2.13
	ch.26	728.37	3.70	716.23	3.83	716.49	4.25	713.04	4.34
	ch.27	726.00	4.03	694.05	2.76	711.69	4.19	701.18	4.00
	ch.28	717.49	4.34	705.01	4.20	719.93	4.66	704.64	6.43
	ch.29	725.96	3.32	698.91	3.47	730.83	4.41	707.22	3.45
	ch.30	724.69	3.24	684.10	3.17	723.99	5.16	703.25	4.18
	ch.31	728.64	3.05	689.76	2.52	723.08	4.71	700.16	5.00

Table B.5.: Mean μ and standard deviation σ of the noise distribution gained from the fit of S-curve for gain 62.

List of Figures

2.1. Previous measurements of the proton radius from electron proton scattering experiments and the Lamb shift in muonic and ordinary hydrogen, the measurements differ from each other by five standard deviations. An arbitrary result for the proton radius by the PRM experiment, with the expected uncertainty, is included.[1]	4
2.2. General setup of the Amber experiment with new detectors for PRM[7]	5
2.3. Unified tracking station (UTS) with three layers of pixilized silicon detectors (ALPIDEs) and the scintillating fiber hodoscope (SFH)[7]	6
2.4. Scintillating fiber hodoscope (SFH) with two of the four layers of scintillating fibers installed. The frontend electronics is not attached[7]	7
3.1. Sideview of the frontend electronics that will be attached on the sides of the SFH, the fiber holders will be attached to the fibers[7]	10
3.2. The analog frontend electronics (FEE) PCB with the six Citiroc1A ASICs. The output of the Citiroc1A ASICs is transmitted to the iFTDC over three flex PCBs[7]	11
3.3. The signals used by the FPGA to control and readout the two Citiroc1A ASICs[14]	11
3.4. General ASIC block scheme of the Citiroc1A[14]	12
3.5. High gain amplification of the Citiroc1A. The feedback capacitance is adjustable from 25 fF to 1575 fF in 25 fF steps[14]	13
3.6. The two configurable registers of the Citiroc1A are selected using the Select signal. The FPGA communicates with the Citiroc1A through the signals Clk_sr , Rstb_sr , Srin_sr , and Load_sr , while the Sroutr signal is sent back from the Citiroc1A to the FPGA for verification[14]	14

List of Figures

3.7. The slow control chronogram, depicting the bitstream writing process controlled by Clk_sr the clock signal and Srin_sr the data signal. A rising edge of Load_sr is required after successful verification with the Sroutr signal to load the slow control register[14]	15
3.8. Scheme block of internal probing system, allowing the routing of internal signals to probe pins for debugging purposes. It is configured via the probe register[14]	16
3.9. The iFTDC with three Artix-7 FPGA, the three flex PCBs that connect the iFTDC with the FEE PCB and the connected power supply.	18
4.1. Hierarchical structure of the firmware, where each module contains its sub-modules. The black arrows indicate connections that are semantically correct but are routed through higher-level modules.	20
4.2. Structure of the status and control register of the Citiroc1A interface. The specified commands are executed when the bits are set to 1.	22
4.3. Finite state machine for configuring the Citiroc1A ASIC. States associated with the same processes are highlighted using the same color.	23
4.4. Finite state machine for verifying the configuration of the Citiroc1A ASIC. States belonging to the same processes are represented with the same color.	25
4.5. Experimental setup for the noise measurement of the frontend electronics of the scintillating fiber hodoscope.	27
4.6. Experimental setup for the noise measurement with an Evaluation Board provided by Weeroc company.	28
5.1. Threshold scan of the Citiroc1A ASICs of FPGA 1 and 2 for gain 58 from threshold 0 to 800.	32
5.2. Threshold scan of the Citiroc1A ASICs of FPGA 1 and 2 for gain 59 from threshold 0 to 800.	33
5.3. Threshold scan of the Citiroc1A ASICs of FPGA 1 and 2 for gain 60 from threshold 0 to 800.	34
5.4. Threshold scan of the Citiroc1A ASICs of FPGA 1 and 2 for gain 61 from threshold 0 to 800.	35
5.5. Threshold scan of the Citiroc1A ASICs of FPGA 1 and 2 for gain 62 from threshold 0 to 800.	36
5.6. Results of the S-curve analysis for channel 0 of Citiroc1A 1 of FPGA 1 with gain 60.	37
5.7. Results of the S-curve analysis for channel 0 of Citiroc1A 1 of FPGA 1 with gain 61.	38

5.8. Results of the S-curve analysis for channel 0 of Citiroc1A 1 of FPGA 1 with gain 62.	38
5.9. Results of the S-curve analysis for all channels of the Citiroc1A ASICs of FPGA 1 and 2 with gain 62.	39
5.10. Mean μ and standard deviation σ determined from the S-curve fits for all channels of the Citiroc1A ASICs of FPGA 1 and 2 plotted vs the gain.	40
5.11. Comparison of the threshold scan of the frontend electronics to the thresh- old scan performed on a by Weeroc company provided Evaluation Board with a gain of 58.	41

Bibliography

- [1] B Adams et al. *COMPASS++/AMBER: Proposal for Measurements at the M2 beam line of the CERN SPS Phase-1: 2022-2024*. Tech. rep. Geneva: CERN, 2019. URL: <https://cds.cern.ch/record/2676885> (cit. on pp. 1, 3–6).
- [2] B. Adams et al. *Letter of Intent: A New QCD facility at the M2 beam line of the CERN SPS (COMPASS++/AMBER)*. 2019. arXiv: 1808.00848 [hep-ex]. URL: <https://arxiv.org/abs/1808.00848> (cit. on p. 4).
- [3] Maxim Alexeev et al. “Design and Testing of a new Tracking System for the Proton Charge Radius Measurement with the AMBER Experiment at CERN”. In: *PoS VERTEX2023* (2024), p. 049. DOI: 10.22323/1.448.0049 (cit. on p. 5).
- [4] E. E. Chambers and R. Hofstadter. “Structure of the Proton”. In: *Phys. Rev.* 103 (5 Sept. 1956), pp. 1454–1463. DOI: 10.1103/PhysRev.103.1454 (cit. on p. 1).
- [5] The AMBER Collaboration. *AMBER Status Report 2024*. Tech. rep. Geneva: CERN, 2024. URL: <https://cds.cern.ch/record/2907624> (cit. on p. 7).
- [6] Procedia Cpi. “Classifying FPGA Technology in Digital Signal Processing: A review”. In: *International Journal of Engineering & Technology Sciences* 2023 (July 2024), p. 10 (cit. on p. 9).
- [7] Karl Eichhorn. Private Communication. Nov. 2024 (cit. on pp. 5–8, 10, 11, 45, 51).
- [8] J M Friedrich and O Denisov. *AMBER Status Report 2022*. Tech. rep. Geneva: CERN, 2022. URL: <https://cds.cern.ch/record/2810822> (cit. on pp. 6, 7).
- [9] Werner Heisenberg. *Physics and Philosophy: The Revolution in Modern Science*. Ed. by Ruth Nanda Anshen. Amherst, N.Y.: Prometheus Books, 1958 (cit. on p. 1).

Bibliography

- [10] P. Kmon, P. Maj, P. Grybos, and R. Szczygiel. “An Effective Multilevel Offset Correction Technique for Single Photon Counting Pixel Detectors”. In: *IEEE Transactions on Nuclear Science* 63.2 (2016), pp. 1194–1201. DOI: 10.1109/TNS.2016.2527834 (cit. on p. 29).
- [11] Igor Konorov. Private Communication. Oct. 2024 (cit. on pp. 2, 9–11, 13, 18).
- [12] C. Ghabrous Larrea et al. “IPbus: a flexible Ethernet-based control system for xTCA hardware”. In: *Journal of Instrumentation* 10.02 (Feb. 2015), p. C02019. DOI: 10.1088/1748-0221/10/02/C02019 (cit. on pp. 19, 20).
- [13] Barrie M. Peake. “The discovery of the electron, proton, and neutron”. In: *Journal of Chemical Education* 66.9 (1989), p. 738. DOI: 10.1021/ed066p738 (cit. on p. 1).
- [14] Weeroc. *citiroc1a-datasheet-v2-53*. Dec. 2019. URL: <https://www.weeroc.com/~documents/products/citiroc-1a/citiroc1a-datasheet-v2-53/?layout=file> (cit. on pp. 11–17).
- [15] R.L. Workman et al. *Review of Particle Physics: 2022*. Vol. 2022. Oxford: Oxford University Press, 2022. DOI: 10.1093/ptep/ptac097 (cit. on pp. 1, 3).

Acknowledgement

I want to thank:

Igor Konorov

For teaching me the basics of FPGA programming and hardware design and for his ongoing guidance throughout this project.

Furthermore, for sharing his office as well as his knowledge and time with me when answering my many questions.

Karl Eichhorn and Dr. Martin Losekamm

For helping me understand how the frontend electronics of the scintillating fiber hodoscope work and supporting me during this thesis.

Dr. Jan Friedrich

For giving me the opportunity to work on such an exciting project, as well as allowing me to work in the AMBER group.

The E-18 group

For the great working atmosphere and the many interesting meetings and discussions that furthered my understanding and knowledge.

Professor Stephan Paul

For welcoming me in the E-18 group and taking the time to read and correct this thesis.

Eidesstattliche Erklärung

Ich versichere hiermit an Eides statt, dass ich die von mir eingereichte Arbeit bzw. die von mir namentlich gekennzeichneten Teile selbstständig verfasst und ausschließlich die angegebenen Hilfsmittel benutzt habe. Die Arbeit wurde bisher in gleicher oder ähnlicher Form in keiner anderen Prüfungsbehörde vorgelegt und auch noch nicht veröffentlicht.

Ort, Datum

Unterschrift